Magnetic Induction Based Energy Harvester for Sensor Networks and Impressed Current Cathodic Protection

by

Xiaoxuan Wang
B.Eng, Harbin Engineering University, 2013

A Project Report Submitted in Partial Fulfillment of the
Requirements for the Degree of

MASTER OF ENGINEERING

in the Department of Electrical and Computer Engineering

University of Victoria

Magnetic Induction Based Energy Harvester for Sensor Networks and Impressed Current Cathodic Protection

by Xiaoxuan Wang

Xiaoxuan Wang
B.Eng, Harbin Engineering University, 2013

Supervisory Committee

Dr. Tao Lu. Supervisor Main, Supervisor
(Department of Electrical and Computer Engineering)

Dr. Prof. Ashoka K. S. Bhat. Member One, Departmental Member
(Department of Electrical and Computer Engineering)

Supervisory Committee

Dr. Tao Lu. Supervisor Main, Supervisor
(Department of Electrical and Computer Engineering)

Dr. Prof. Ashoka K. S. Bhat. Member One, Departmental Member
(Department of Electrical and Computer Engineering)

ABSTRACT

For electric power transmission system, the electro-magnetic energy along the high voltage transmission line can be collected by an energy harvester. This makes the harvester a feasible candidate to power up the sensors deployed in power grids. In this report, a design of magnetic induction based energy harvester is demonstrated with the inclusion of derivations of formulas, discussions of chosen materials and steps of creating geometry model using SolidWorks. Modeling and simulation of the energy harvester using COMSOL and LTspice are also explained along with the analysis of the results. In addition, cathodic protection of steel towers in power networks powered by the proposed energy harvester is investigated. In particular, the impressed current cathodic protection method, its principles of operation, thermodynamic behavior and simulation approached are illustrated. Finally a system integration of energy harvester and impressed current cathodic protection system that can not only monitor the environment of power grid but also prevent corrosion in steel tower is proposed.

Contents

List of Tables

List of Figures

ACKNOWLEDGEMENTS

First, I would like to thank my supervisor Dr. Tao Lu, for his great guidance and patience that help me studying the whole learning program. The academic and research attitude of him inspire me learn and understand the engineering study process and creative thoughts for solving problem.

Second, I would like to thank Giuseppe Stanciulescu, our collaborator from BC hydro for the inspiring guidance on this project.

Also, I would like to thank my colleagues, Wen Yan, Wen Zhou, Liao Zhang, He Ma and Han Xiao of our group in University of Victoria.

Last, I would like to thank Bo Han who always support me.

DEDICATION

To my loved parents, who are always by my side.

Chapter 1

Introduction

To maintain the normal operations of the electricity power system, a variety of performance monitoring data are collected from sensors deployed within the infrastructure. Consequently, stable and low-cost power supplies are required to power the corresponding sensors. Furthermore, corrosion occurs on the steel tower supporting the power transmission lines, which costs a substantial budget every year for repair. An effective method that can prevent corrosion powered by the proposed harvester will be discussed in this thesis.

1.1 Energy Harvester

An energy harvester is a device that acquires thermal, electromagnetic, wind or solar energy from an external source to support electric devices. The energy source for a harvester is typically natural, sufficient and sometimes redundant to make the harvester low-cost and energy efficient.

In the past, a variety of energy harvesters have been demonstrated in a wide range of applications. For example, a micro-power photovoltaic module was built to provide electrical power to an autonomous gas sensor through an energy efficient solar energy harvester[1]. He, et.al. demonstrated that a piezoelectric harvester containing a cantilever beam and magnetic circuit can collect energy from alternating current (AC) magnetic field emitting from a high voltage power line [2]. An auto-parametric resonance vibration energy harvester based on resonant amplification was developed by Yu et. al.[3]. Horowitz et. al. introduced a micro-machined acoustic energy harvester producing a maximum output power density of 0.34 μW/cm^2 at 149 dB

Figure 1.1: Solar Panels (Reprinted from[7]).

acoustic input [4]. Also, a semi-flexible bimetal-based thermal energy harvester can transfer thermal gradients into electricity, with an output power of 13.46 μW per device from a 60° C thermal source [5]. On the other hand, a maximum of 3.99 mW output power can be produced by a wearable thermal energy harvester powered by human foot of an adult standing on room temperature ground[6]. Dias et. al. presented a thermoelectric a solar energy harvester based on a solar panel to power a multi-sensor system for agriculture[8]. A schematic of such solar panel is illustrated in Figure 1.1[7].

Figure 1.2 [9] shows a piezoelectric energy harvester that utilizes the basic piezoelectric beam for powering circuits or sensors. It can be applied to a cardiac pacemaker[10], or even a bicycle[11] to make them self-powered. Another example is the auto-parametric energy harvester that contains a pendulum and an excited oscillator at its low-frequency vibration [12]. In addition, Aldraihem and Baz presented a harvester consisting a dynamic magnifier between the piezoelectric element and moving base to improve the strain of the piezo-element and increase the output power of the energy harvester[13]. An electromechanical energy harvester with a magnet held by a spring can produce a normalized power density of 1.7 μW$/(m/s^2)s^2cm^3$ at a resonance frequency of 112.25Hz [14]. The schematic of the electromechanical energy harvester with a magnet is shown in Figure 1.3.

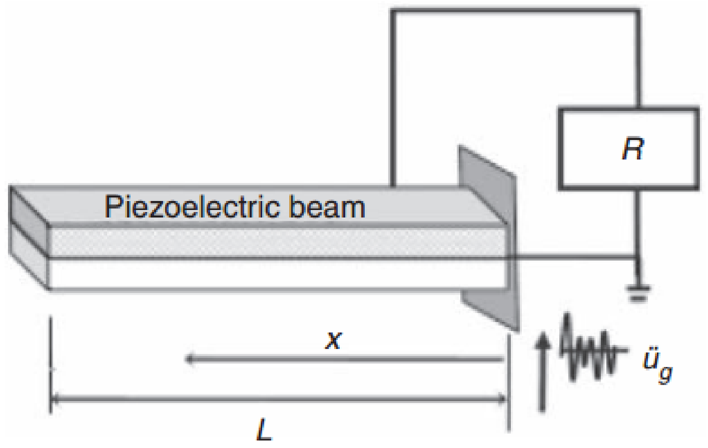

Figure 1.2: A piezoelectric energy harvester example (Reprinted from [9]).

In this thesis, we investigate the energy harvester that is suitable for providing stable power to performance monitoring sensors and steel tower corrosion prevention system. One candidate of such energy harvester would be a solar energy harvester. However, the performance of a solar energy harvester relies heavily on the weather. Such harvesters do not function at its full capacity during cloudy and rainy days, thus is unsuitable for desired applications. On the other hand, a magnetic induction based harvester provides constant energy to power sensors and batteries as long as there is steady and sufficient AC flowing through the conductor of a high voltage transmission line. As Figure 1.4 shows, the magnetic induction based energy harvester or energy coupler is placed on the high-voltage transmission line. The AC flowing through the conductor generates an inductive voltage on the terminals of the coils in the energy harvester and will be converted to DC by the rectifier installed in the harvester. The output DC will then be used as the energy source for the sensors and corrosion protection.

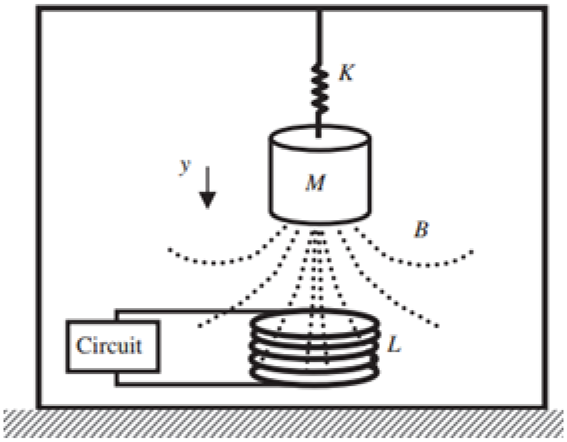

Figure 1.3: Schematic diagram of magnetic induction energy harvester (Reprinted from [14]).

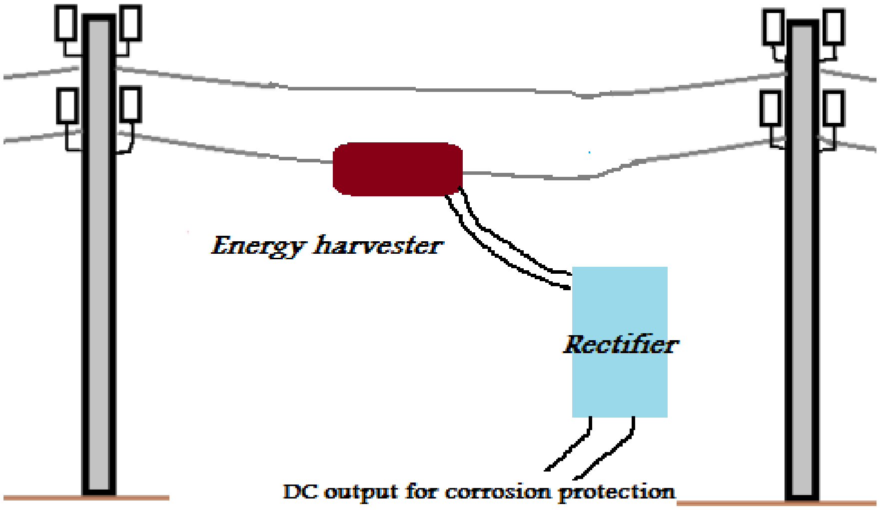

Figure 1.4: Schematic diagram for magnetic induction harvester.

1.2 Cathodic Corrosion Protection

Corrosion of the industrial infrastructures costs over one trillion dollars (6.2 percent of GDP) in the US according to the National Association of Corrosion Engineers (NACE) report [15]. More specifically, BC Hydro spends 530,000 dollars yearly on repairing the corroded steel towers. Evidently, corrosion protection is of key interests for BC Hydro to manage their infrastructure.


(a) Corroded ship propeller [16]
(b) Corroded pipelines [17]

Figure 1.5: Examples of corrosive metals.

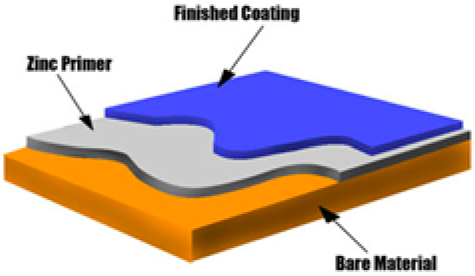

Figure 1.6: An example of coating using zinc (Reprinted from [18]).

When corrosion occurs, it will reduce strength and other properties of the structure. This is exemplified in Figure 1.5 for corroded ship propellers (a) and pipelines (b).

One approach to prevent corrosion is to apply coating on the surface of the metal as illustrated by Figure 1.6. It includes two steps of coatings, zinc is first coated due to its relative stable property, and a finish coating is applied to get a better exterior [18].

For structures such as oil pipes, gas transport tubes, and marine facilities, cathodic protection is a solution to metallic corrosion prevention. The metallic structure is set as a cathode in an electrochemical cell in cathodic protection so that it can be protected through further steps. Figure 1.7 illustrates the chemical reactions on the metal when corrosion takes place, the anode part will lose electrons and ions while the hydrogen is generated on the cathode part. Further, oxides of irons will be generated

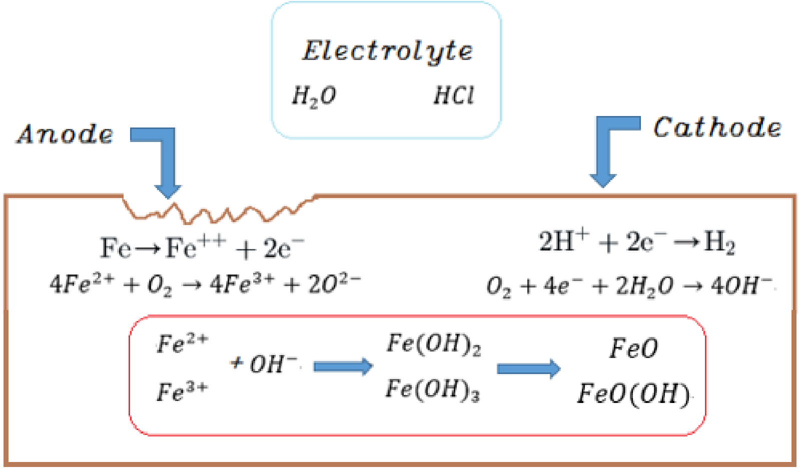

Figure 1.7: Chemical reactions on metal when corrosion occurs.

on the anode part which makes the metal rusty.

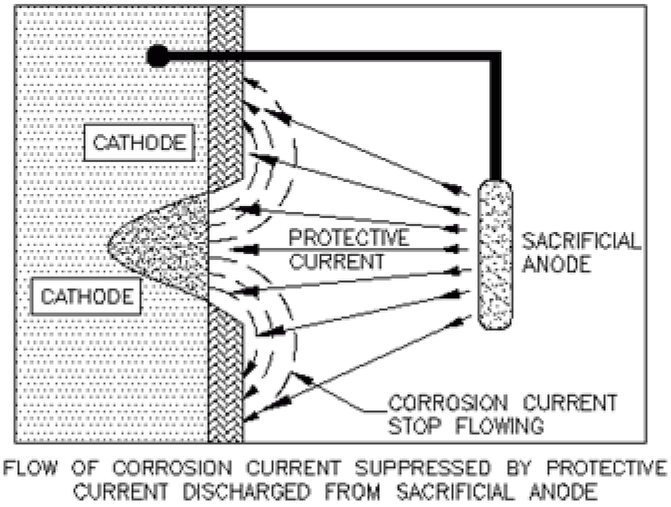

Figure 1.8: Schematic diagram of sacrificial anode cathodic protection system. (Reprinted form [16])

There are two main methods for cathodic protection. One is simply connecting an anode with the structure in the electrolyte as illustrated in Figure 1.8, forming an electrochemical cell along with the cathode part. When the metal chosen for the anode is much more *active* than the cathode, it will lose electrons due to the potential difference between the electrode and metal. Consequently, the electrons will flow across the cable to the cathode to fill in the cathode. In this process, the anode, also named as the sacrificial anode, loses electrons and ions to the cathode and requires the replacement of anode every period.

The other type of cathodic protection is called *Impressed Current Cathodic Protection*(ICCP). It contains anodes connecting to a rectifier to convert AC to DC. The anode can be made from a variety of materials including graphite, silicon cast iron, platinum, magnesium, etc. It is connected to the positive port of the rectifier, while the structure to be protected is connected to the negative port. The DC power provides a voltage higher than the sacrificial anode system to imitate a much stronger anode that impresses current from the anode to the cathode. This makes the potential between anode and cathode larger than that of corrosive reaction on the structure. Consequently, the cathode will be protected. Compared to the former approach, ICCP makes the lifetime of the protected structure significantly longer. In addition, the installation process is simple since it only requires the settings around the anodes, backfill and the connection to the rectifier. It is worth mentioning that ICCP system requires constant monitoring in order to adjust the input current based on the potential of surface, salinity of the sea water or humidity of the earth.

As illustrated in Figure 1.9, ICCP is frequently adopted to protect a steel tower by making it as the cathode in an electrochemical cell connected to the rectifier with a cable and anodes with an electrolyte. Also, with a similar design, cathodic protection can be feasible and cost friendly by harvesting energy from the transmission line [19].

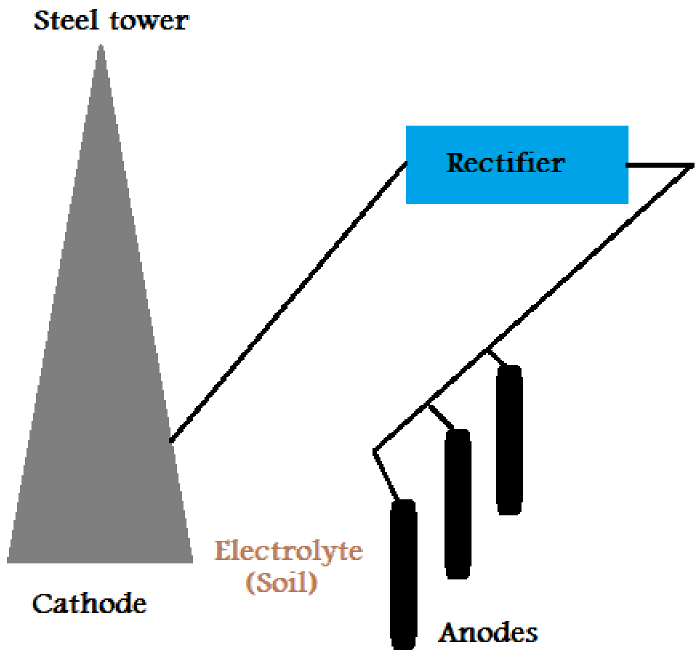

Figure 1.9: Model for impressed current cathodic protection for steel tower.

To summarize, in our system, we choose ICCP for corrosion protection, the energy is collected from the high voltage transmission line through an energy harvester and converted into DC power by a rectifier circuit. The proposed harvester can be used for powering wireless sensors and protecting the corrosion that may happen on steel structures in the electric power grid.

1.3 Thesis Outline

The outline of this project report is listed below:

Chapter 2 Introduce the basic principle of magnetic induction and the design for energy harvester.

Chapter 3 Demonstrate the principle of impressed current corrosion protection method, the thermodynamics theory of electrochemical cells and how to determine the number of anodes.

Chapter 4 Numerical implementing methods for creating geometry model and setup for simulation both in energy harvester and corrosion protection.

Chapter 5 Results analysis for induced voltage and current density from energy harvester.

Chapter 6 Results analysis for impressed current corrosion protection.

Chapter 7 Conclusion and future work.

Chapter 2

Energy Harvesters Based on Magnetic Induction

Among all energy harvesters, magnetic induction energy harvester is advantageous for its stable power provision, relatively low cost, and simple installation. In this chapter, principles of magnetic induction harvesting are explained. In addition, rectification circuits used for converting the harvested inductive voltage are demonstrated with simulation.

2.1 Basics of Magnetic Induced Energy Harvester

A magnetic induced energy harvester consists a current transformer and an AC-DC converter. The current transformer is used for generating induced voltage from alternating magnetic field around the high-voltage transmission line. At the terminals of its coils, the current lags 90° phase behind the applied voltage as shown in Figure 2.1.

When a transmission line carries AC, an alternating magnetic field is created around the conductor. Therefore, the generated AC induced voltage at the terminals of the conductor can be analyzed as a series LR circuit shown in Figure 2.2. Here the impedance Z can be expressed as: $Z = R + jX_L = R + j\omega L$, X_L is the reactance of the coil, R is the resistance, $\omega = 2\pi f$ is the angular frequency of the AC source, f is the frequency, and L is the inductance.

The total voltage(V) at coil terminals can be expressed by using a vector triangle: $V^2 = V_L^2 + V_R^2$, where V_R and V_L are the voltages on the resistor R and coil L,

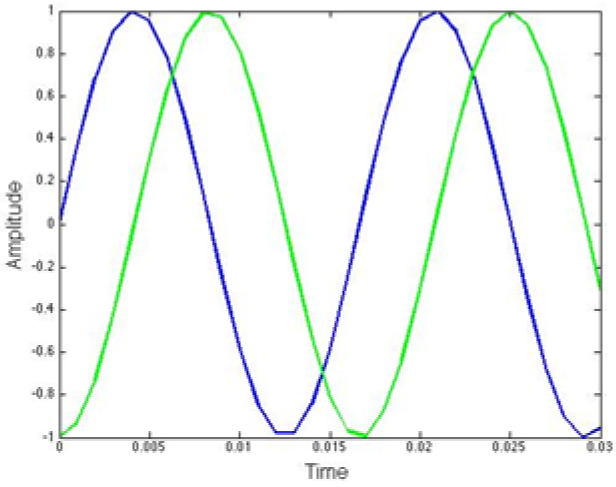

Figure 2.1: Voltage leads current by 90° in phase in AC circuit. (Blue curve represents voltage of the coil, green curve represents current of the coil).

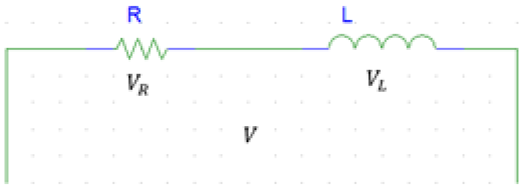

Figure 2.2: Series LR combination

respectively. By simple substitution, we obtain: $V = I\sqrt{R^2 + X_L^2}$, where I is the current flowing through the series LR circuit.

Inductance is used to describe how the coil react to the alternating current flowing through it. From the magnetic circuit shown in Figure 2.3, inductance can be described as:

$$L = N\frac{d\phi}{di} \tag{2.1}$$

where N is the number of turns of the coil, ϕ is the flux the current creates, i is the current that goes through the conductor.

The induced voltage at the terminals of the coil can be expressed as:

$$V = L\frac{di}{dt} \tag{2.2}$$

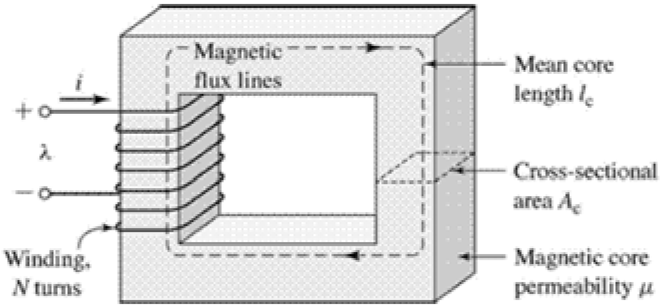

Figure 2.3: Magnetic circuit (Reprinted from [20]).

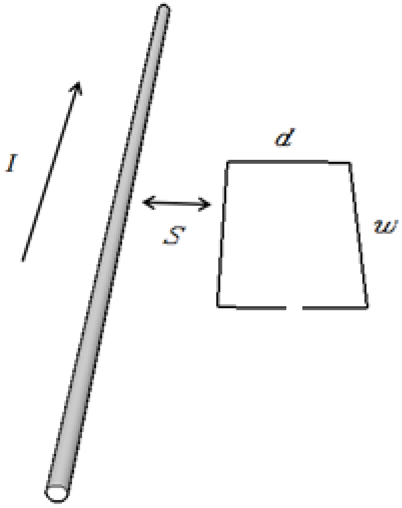

Figure 2.4: AC current going through the wire while a rectangular coil located beside it.

Based on the Faraday's law, the amount of induced AC voltage generated on the coil terminals depends on the relative permeability of the medium, the current flowing through the conductor, the distance between the coil and the conductor, and the size of the coil. As shown in Figure 2.4, the harvester can be modelled as a rectangular coil located next to a current-carrying wire. Here the distance between rectangular coil and the straight wire is s, the width and length of coil are d and w, respectively. μ_0 is the permeability of free space, μ_r is the relative permeability of medium, and $i = I_p \sin(\omega t)$ is the AC current source with I_p the peak value of the input current source. The magnetic flux in the coil can be calculated by: $\phi = \int_s^{s+d} \frac{\mu_0 \mu_r i}{2\pi r} w dr = \frac{\mu_0 \mu_r w i}{2\pi} ln(1 + \frac{d}{s})$. The output voltage at the terminals of the

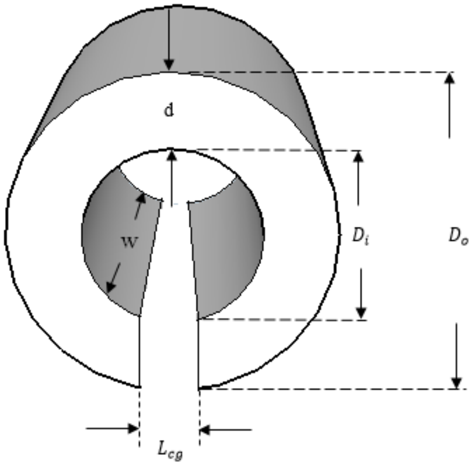

Figure 2.5: The structure of the magnetic core for energy harvester.

coils can be obtained by substituting magnetic flux expression into induced voltage expression below,

$$\begin{aligned} V &= -N\frac{d(\frac{\mu_0\mu_r wi}{2\pi}ln(1+\frac{d}{s}))}{dt} \qquad (2.3) \\ &= -N\frac{\mu_0\mu_r w}{2\pi}ln(1+\frac{d}{s})\omega I_p\cos{(\omega t)} \end{aligned}$$

Since the root mean square value of $I_p\cos{(\omega t)}$ is the same as $i = I_p\sin{(\omega t)}$, the root mean square value voltage at the terminals of the coils should be:

$$V_{rms} = N\mu_0\mu_r wfIln(1+\frac{d}{s}) \qquad (2.4)$$

According to Eq.(2.4), a multi-turns coil can be used for harvesting energy from an AC current carrying conductor. To hold the coil and increase the medium permeability, a hollow cylinder magnetic core should be applied as shown in Figure 2.5. In addition, a core gap is designed to make energy harvester much easier to install on the high voltage transmission line.

In practice, the impact of the core gap to the effective permeability must be taken into consideration. Given the inner D_i and outer diameter D_o of the hollow cylinder in Figure 2.5, the core gap length can be calculated as[21]:

$$L_{cg} = \frac{\pi(D_o - D_i)}{ln(\frac{D_0}{D_i})} - L_m \qquad (2.5)$$

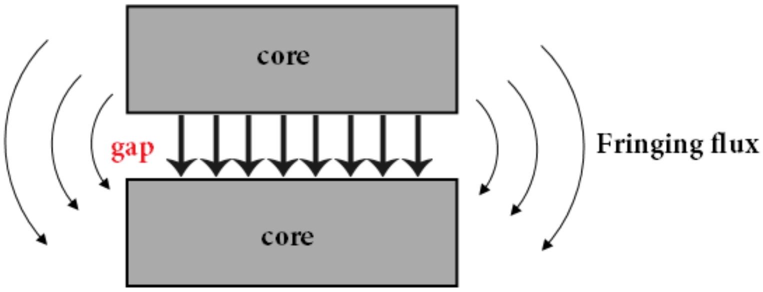

Figure 2.6: Fringing flux happens at core gap.

where L_m is the mean length of the magnetic path of the magnetic core, L_{cg} is core gap length.

It is worth mentioning that, the effective core gap length is much wider than the actual gap due to the effect of fringing flux (c.f.Figure 2.6). Therefore, the effective permeability μ_e of magnetic core can be described as[22]:,

$$\mu_e = \frac{C}{\frac{1}{\frac{A_g}{Lcg}+(0.241+\frac{1}{\pi}ln\frac{b}{Lcg})P}+\frac{C}{\mu_r}} \tag{2.6}$$

where $C = \frac{L_m}{A_g}$, A_g is the cross-section area of the magnetic core, $P = 2(h + w)$ and b=$\frac{\pi D_i}{2}$.

Figure 2.7 illustrates a 3D model of energy harvester based on the rectangular coil. As shown, a magnetic core wounded by multi-turns coil is placed on the cable. When the AC flows through the conductor, the open circuit output induced voltage on the terminals of the coil V follows Eq. (2.3), and V_{rms} follows Eq.(2.4).

A more practical simulation of the energy harvester will be introduced in Ch.4 and Ch.5, the simulation result is compared with the ideal case in Ch.5.

2.2 Magnetic Materials

2.2.1 Magnetic properties

Magnetic core is a key issue for magnetic induced energy harvester since the property of the material determines the performance of the harvesting efficiency. Materials with high permeability, low loss and high ductility are suitable for magnetic induced

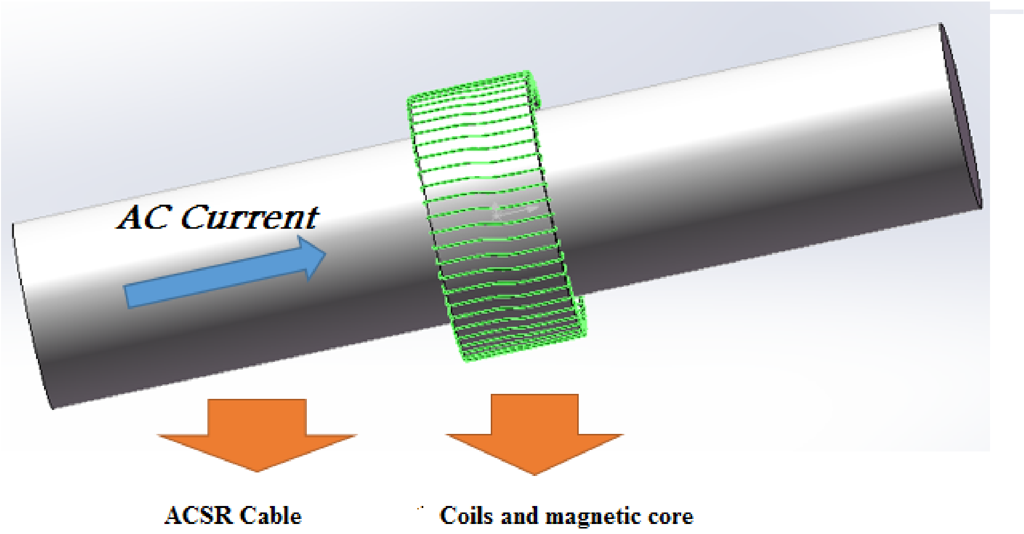

Figure 2.7: Energy harvester structure contains an ACSR cable going through a magnetic core wounded by multi-turns coil.

energy harvesters. Normally, magnetic materials can be grouped on susceptibility χ, which can be expressed as:

$$\chi = \frac{M}{H} \tag{2.7}$$

Here M is the magnetization, H is the magnetic field, both in units of amperes per meter.

Materials such as gold, silver, copper and beryllium with $\chi \leq 0$ are called diamagnetic materials. Diamagnetism is a property of some magnetic material's response to the magnetic field that is similar to paramagnetism and ferromagnetism but at a smaller magnitude. Since the susceptibility of diamagnetic material is negative, the induced magnetic field created in the material will be repelled by the external magnetic field.

Paramagnetic materials have a positive and small susceptibility χ. Its internal magnetic field aligns to the external magnetic field. Materials such as aluminum, molybdenum, titanium and platinum are paramagnetic materials.

Ferromagnetic materials are popularly used almost everywhere for its outstanding properties that allow magnetic induction based devices work effectively. Ferromagnetic materials, including nickel and iron, have much larger susceptibility and permeability. They are used for engineering devices such as electric motors, transformers that require high sensitivity to the electromagnetic field.

The relative permeability of the ferromagnetic materials is not a function of magnetic field strength as oppose to that of the paramagnetic materials. However, it can be expressed by a hysteresis curve that measures the magnetic induction B(Tesla) as a function of magnetic field strength H(amp/m). Hysteresis in the ferromagnetic material is a phenomenon that the magnetic dipoles are aligned by the magnetic field and remain in the arrangement even after removing the external magnetic field.

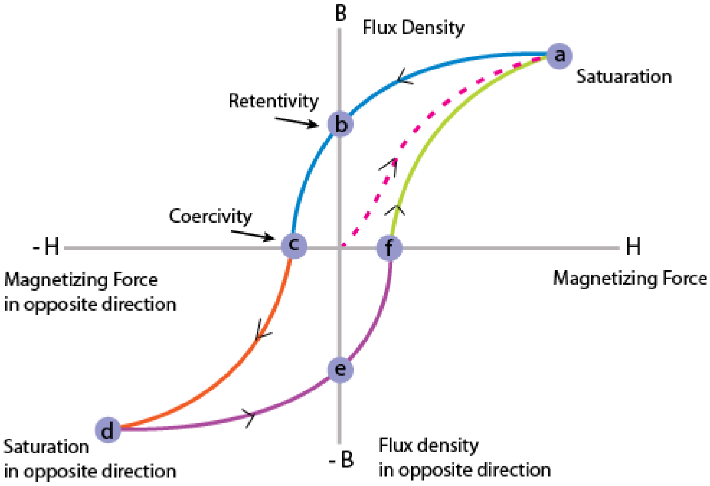

Figure 2.8: Hysteresis loop (Reprinted from [23]).

A hysteresis loop is illustrated with its processes in Figure 2.8, where magnetization saturates at point '*a*'. The magnetic induction B will fall to point '*b*' with the decrease of H. The distance between point '*b*' and the origin is called '*remanence*'. The distance from point '*c*' to '*f*' is twice as coercivity, which describes the amount of magnetic field strength need to reduce the magnetization of the ferromagnetic material. To measure and plot the hysteresis loop, magnetic flux can be recorded with a varying magnetic induction by using tool such as B-H analyzer.

2.2.2 Mu-Metal

The material chosen for magnetic core of the magnetic induction energy harvester is called Mu-Metal, named after its high permeability, low coercivity, and high ductility. It is sensitive to the external field and widely used for transformers. A Mu-metal is a nickel-iron alloy that contains 77 percent nickel, 16 percent iron, 5 percent molybdenum and chromium [24]. Nowadays there are Mu-metals containing more portion of nickel and molybdenum but less portion of iron and copper to increase the permeability. According to Figure 2.10, the coercivity and remanence of Mu-metal are small and the hysteresis loop is much ‘thinner’than most of other magnetic materials’ hysteresis loop. This implies that mu-metal is much more sensitive to the external magnetic field among magnetic materials, making it a perfect material for magnetic induction. In addition, the core gap applied in the energy harvester compromises the effective permeability of the core. This can be compensated by applying Mu-metal with over 100,000 permeability.

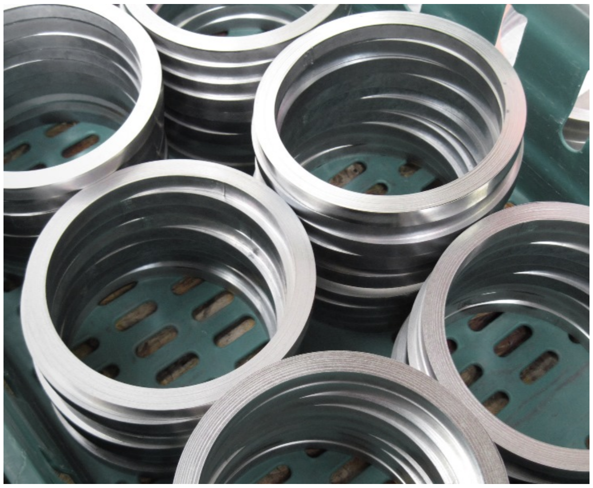

Figure 2.9: Mu-metal toroidal core (Reprinted from [25]).

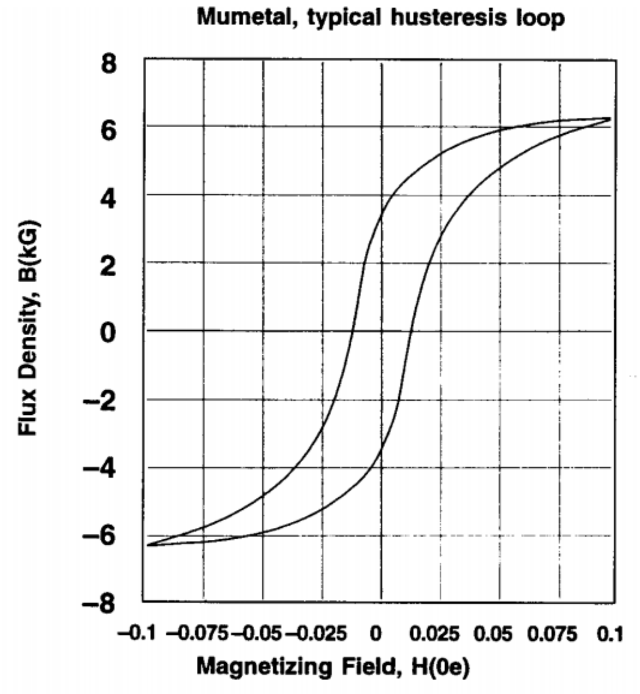

Figure 2.10: Hysteresis loop of mu-metal which shows low coercivity that is suitable for electric motors or transformers (Reprinted from [26]).

2.3 AC-DC Converter

Another part of the energy harvester is the AC-DC converter designed to convert AC induced power into a proper DC voltage for powering sensors and corrosion protection. Rectifiers are used in energy harvester for converting the AC induced voltage to DC voltage. This process is called rectification. Rectifiers have various types, including solid state diodes, vacuum diodes, mercury-arc value, selenium and silicon semiconductor rectifiers, etc [27].

Rectifier circuits can be divided into half-wave rectification and full-wave rectification. Since the full-wave rectification can be more effective, it is tested as an example.

Full wave rectifier can convert an alternating current into a unidirectional output to make full use of both half-wave from one period of input sine wave and to increase the average output power. For example, a full-wave rectification circuit containing four diodes set as bridge configuration input by a 60Hz, 5V peak AC voltage source is shown in Figure 2.12. The output voltage of full-wave rectifier can be simulated by LTspice, which is given in Figure 2.11.

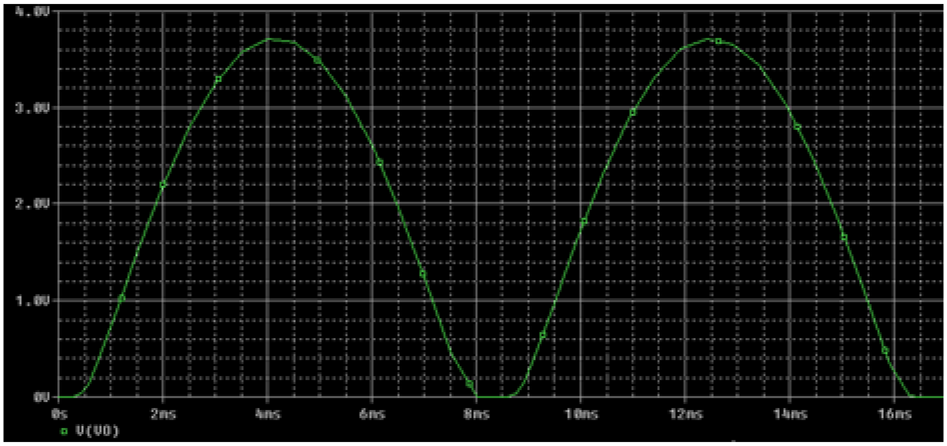

Figure 2.11: The output of full wave rectifier supplied by a 60Hz AC source.

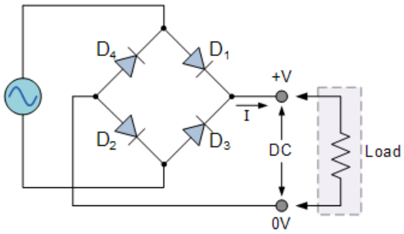

Figure 2.12: Full-wave rectifier circuit created by LTpice.[28]

Based on the full-wave rectification, voltage doubler is a rectifier that converts the input AC voltage to output twice in magnitude in the ideal case. In practice, due to the load resistance, the rate of output DC voltage over the peak value of AC input voltage are smaller than two.

Delon circuit is introduced as shown in Figure 2.13. Different from the full-wave rectifier, the diodes in Delon circuits are connected in series, along with two capacitors in bridge which is called doubler. A test simulation of Delon circuit is done by LTspice with 60Hz, 5V amplitude AC input set for V1. The result for both input voltage(V_i) and output voltage(V_o) are displayed and compared in Figure 2.14.

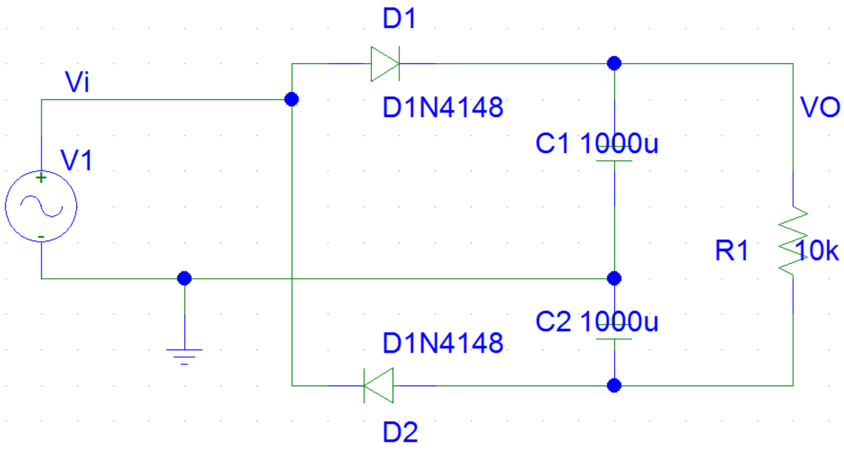

Figure 2.13: Delon circuit.

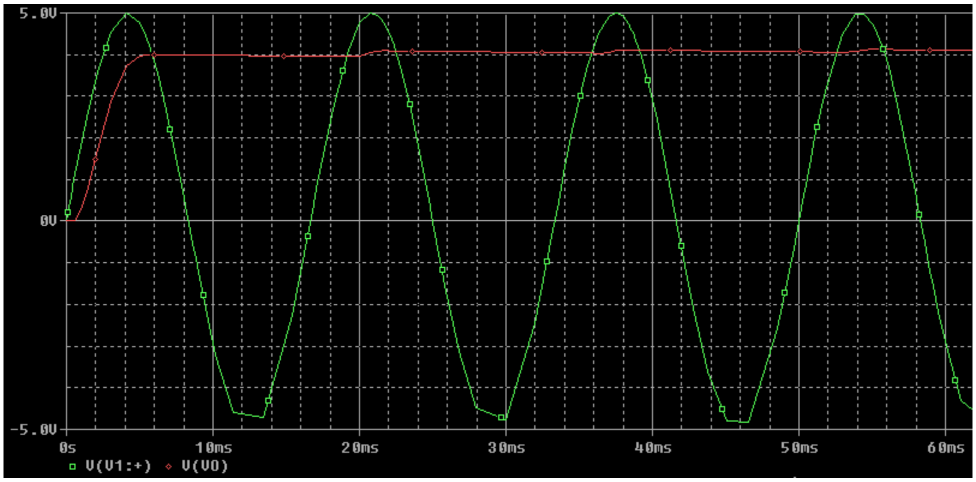

Figure 2.14: The output at point VO of Delon circuit (red curve) compared with the result tested at point Vi as labeled in Figure 2.13.

The output voltage of Delon circuit can be expressed as a form of input peak voltage and voltage drop of the diodes: $V_0 = 2V_i - 2V_D$.

It can be indicated from Figure 2.14 that the output of the circuit rises from 0V to about 4.1V in about 20ms, the output becomes stable after that. The ratio of the output voltage to the root mean square value of the input is only 1.186 due to the considerable forward voltage drop of diodes. Therefore, a voltage quadruapler is tested since the low ratio may not be enough for powering sensors.

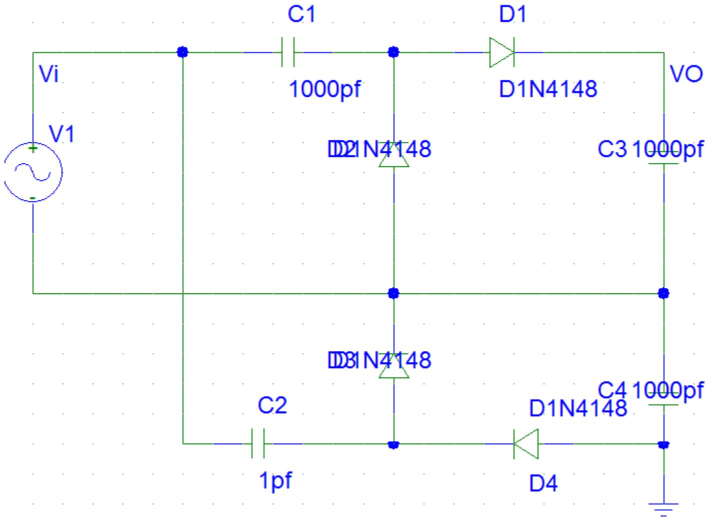

Figure 2.15: Voltage quadrupler circuit.

Figure 2.15 illustrates the circuit of voltage quadrupler that combines two doublers, that provides quadruple output as input with respect to the ground.

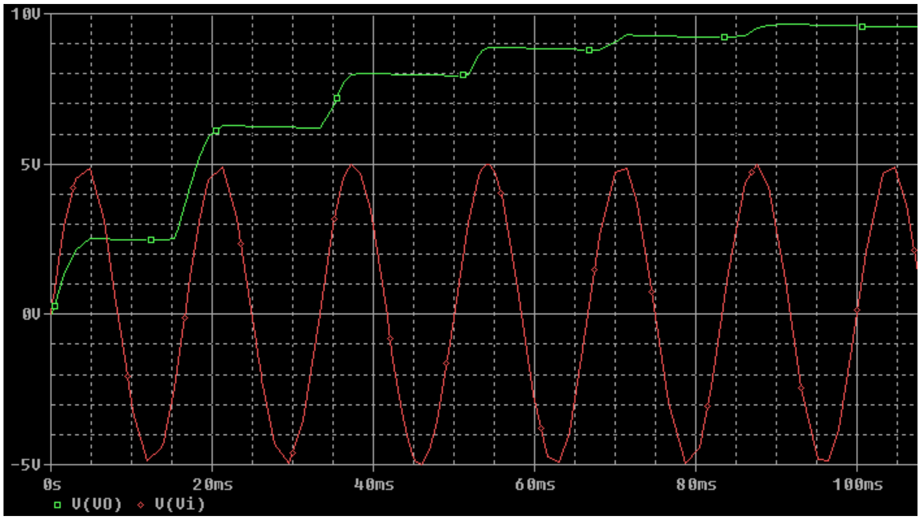

Figure 2.16: Output and input voltage diagram from 5V amplitude AC source that going through a voltage quadrupler.

Figure 2.16 shows the test result for voltage quadrupler with input 5V AC voltage that produces a DC output at about 9V that is only almost twice as input. Obviously, both voltage doubler of Delon circuit and voltage quadrupler output have considerable losses. The main reason is that the voltage drop caused by the diodes, each silicon diode will cause 0.7V voltage drop. In addition, the dissipated energy heats up the energy harvester constantly and reduces the service life of the device. To avoid the diode voltage drop, active diode consisting a MOSFET and a comparator shown in Figure 2.17 is introduced for its lower turn-on voltage compared to the junction based diode used in voltage multiplier mentioned before[29][30][31].

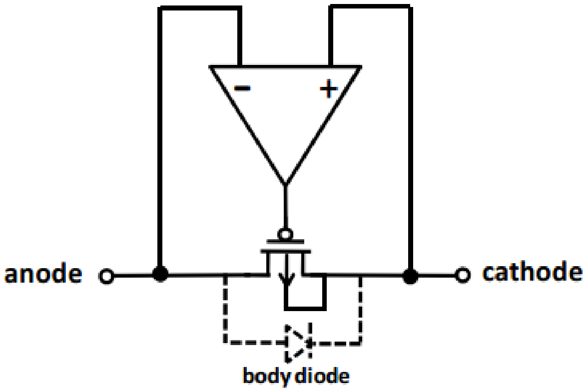

Figure 2.17: Active diode (Reprinted from [32]).

The main loss of active diode is caused by the resistive and conductive loss of the PMOS and the power consumed by the comparator [32]. PMOS is p-channel MOSFET(metal-oxide-semiconductor field-effect transistor) that contains n-type substrate, while NMOS(n-channel MOSFET) contains a p-type substrate. Compared to the voltage drop of junction based diode, the conductive voltage drop is much smaller. Choosing a low power cost comparator can make the active diode superior to the diode. From Figure 2.17, when the voltage of the cathode is higher than the anode, the comparator can outputs a low voltage to turn on the PMOS. Similarly, the PMOS is turned off when the voltage of the anode is higher than the cathode. This behavior of the active diode makes the cutting negative input process in rectifier much more efficient.

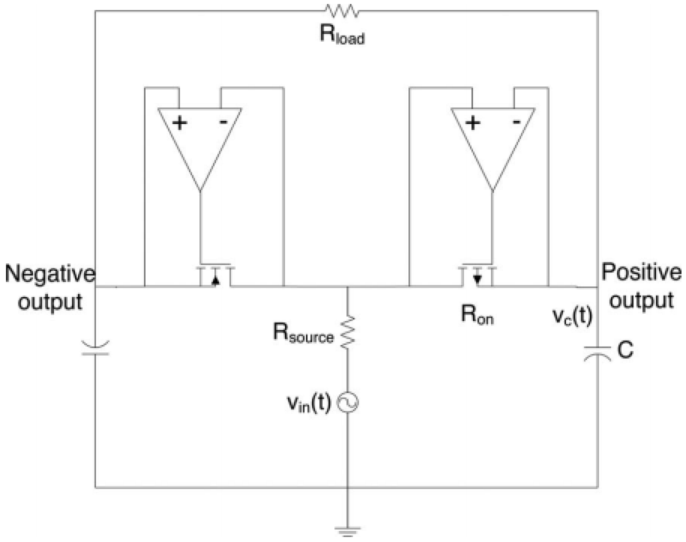

Figure 2.18: Schematic of the active diode voltage doubler (Reprinted from [33]).

Figure 2.18 illustrates the schematic of an active diode voltage doubler to increase the efficiency of the rectifier for an energy harvester. The drain port of one PMOS and the source port of the other PMOS are connected to the input voltage, while the rest ports of the two PMOS are connected to capacitors. A positive output along with a negative output can be tested as shown in Figure 2.18, the output voltage will be the difference between positive and negative output. Therefore, the output voltage applied to the load can obtain nearly twice as input. The test result of positive voltage output is given in Figure 2.19.

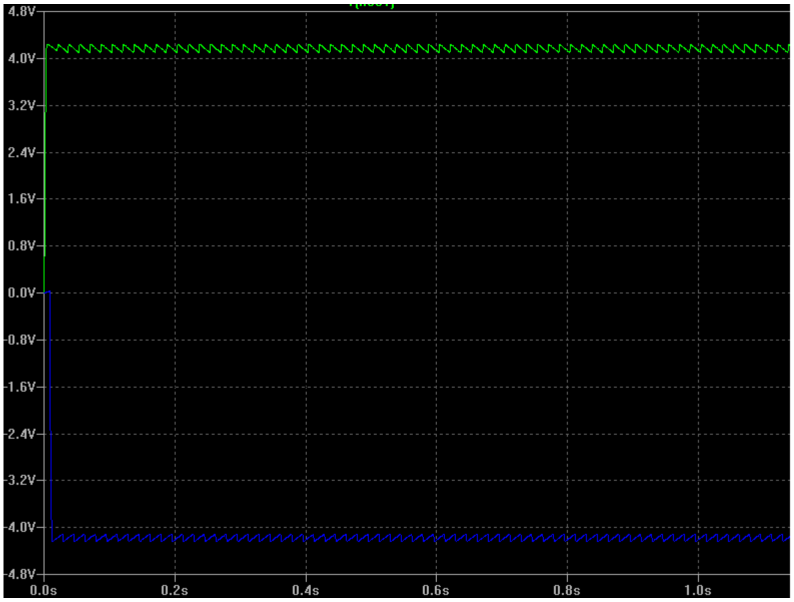

Figure 2.19: Voltage outputs of active diode voltage doubler given a 5V, 60Hz AC input.

In Figure 2.19, both positive (green line) and negative (blue line) output results are plotted. The output DC voltage applied on the 1,000Ω load is 8.32V with an AC-DC converter efficiency of 60.94 percent. This is much more efficient than the voltage doubler of Delon circuit with output no more than 5V peak. The efficiency of converter can be calculated by:

$$\eta = \frac{P_{out}}{P_{in}} = \frac{\frac{V_{out}^2}{R_L}}{\frac{1}{T}\int_0^T v_{in}(t) i_{in}(t) dt} \tag{2.8}$$

where P_{out}, P_{in} are output and input average power. In addition, an AC-DC converter that uses two NMOS for its bidirectional current conductive ability was presented [34], and was improved by Dayal et al. by using a NMOS and PMOS pair to avoid the requirement of floating gate drivers[35]. Similar to the active diode voltage doubler, a bidirectional switch connecting the drain of NMOS to the source of PMOS is applied in the converter shown in Figure 2.20.

In this PMOS and NMOS pair configuration, there are totaly four cases for both positive half cycle input and negative half cycle. For positive half cycle:

1. When both of the NMOS and PMOS is 'ON', the inductor current increases.
2. When NMOS is 'ON', PMOS is 'OFF', the current can flows through the body

diode of PMOS and NMOS, which make the total switch 'ON', the inductor current increases.

3. When NMOS is 'OFF', PMOS is 'ON', current is blocked by the body diode of the NMOS, the total switch is 'ON'. Therefore, the diode D1 is forward biased, the current will charge the C2.

4. When both of the MOSFETS are 'OFF', similarly to the former case, C2 will be charged.

For negative half cycle:

1. When both of the NMOS and PMOS is 'ON', the inductor current increases but in the opposite direction.

2. When NMOS is 'OFF', PMOS is 'ON', the current can flows through the body diode of PMOS and NMOS, which make the total switch 'ON', the inductor current increases.

3. When NMOS is 'ON', PMOS is 'OFF', current is blocked by the body diode of the PMOS, the total switch is 'ON'. Therefore, the diode D2 is forward biased, the current will charge the C3.

4. When both of the MOSFETS are 'OFF', similarly to the former case, C3 will be charged.

Therefore, in the ideal case, the voltage applied on the C1 will be twice as the peak value of the input AC voltage.

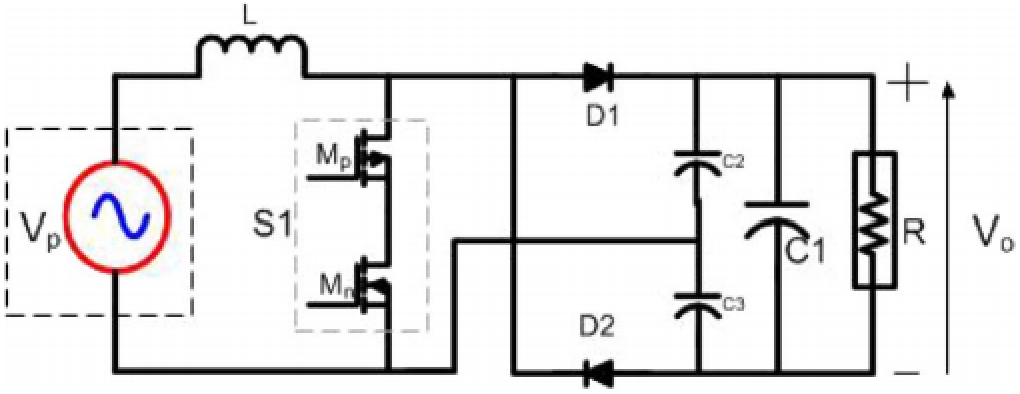

Figure 2.20: Circuit diagram of split capacitor ([35]).

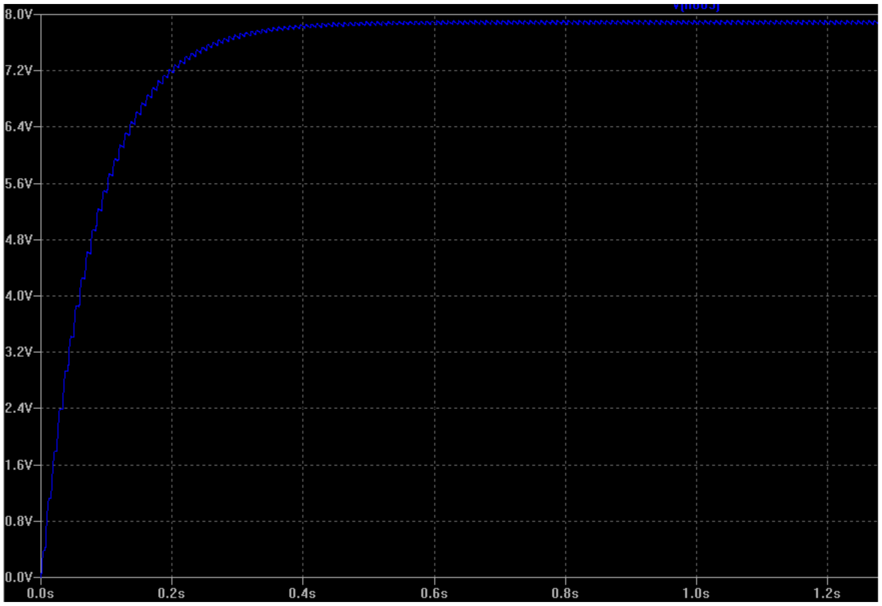

Figure 2.21: Positive voltage output of active diode voltage doubler given a 5V, 60Hz AC input.

From Figure 2.21, the applied DC voltage on 1,000Ω load reached roughly 7.88V along with 72.01 percent rectifier efficiency calculated from Eq.(2.19).

Chapter 3

Impressed Current Cathodic Protection

After the DC voltage is harvested from the high voltage transmission line, it is ready to be utilized directly to power up monitor devices. In addition, the induced current can be applied for corrosion prevention for steel tower based on impressed current cathodic protection method. In this chapter, the principles of the electrochemical cell, thermodynamics of electrochemical reaction and the setting of anodes in ICCP(Impressed current cathodic protection) system are demonstrated.

3.1 Thermodynamics of electrochemical reaction

3.1.1 Basic of electrochemical cell

Impressed current cathodic protection method is widely used for protecting metallic structures such as pipelines, storage tanks and ship hulls that are buried in the electrolyte (soil or sea water). The schematic of impressed current cathodic protection is illustrated in Figure 3.1. The anode is connected to the positive port of converter, while the cathode is connected to the negative port, letting the converter output push the current to the anode and then to the cathode through the electrolyte. This current will be much stronger than the corrosion current flow as shown in Figure 1.8. Hence, the corrosion will be prevented. In a practical ICCP system, the converters are often designed to be regulated by a variable resistor to make the output current suitable for variable conditions. Compared to sacrificial anode system, the impressed current system can protect the surface of the metallic structure with more uniform

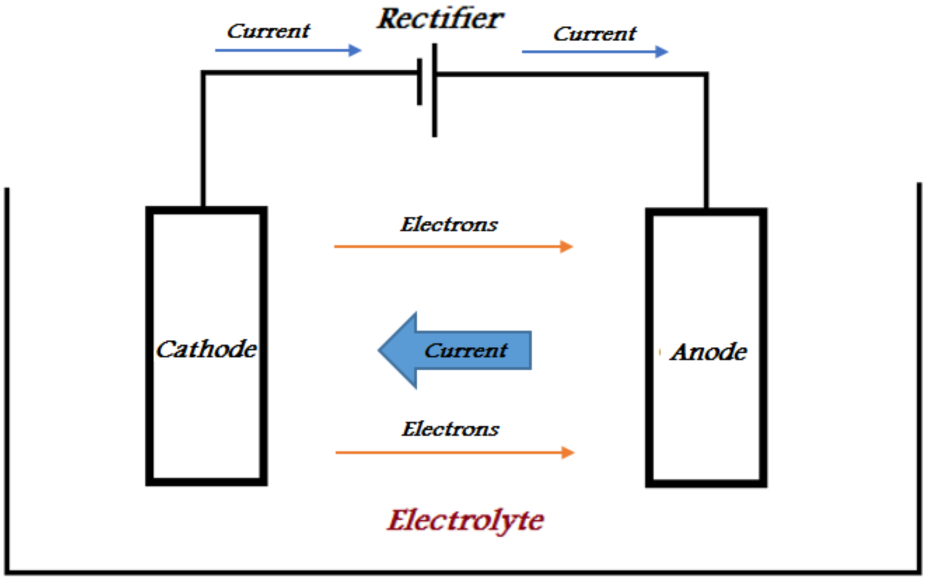

Figure 3.1: ICCP schematic diagram.

potential distribution while consuming less fuel [36]. However, the cost of installing the ICCP system is much higher.

From Figure 3.1 the basic idea of corrosion protection is based on an electrochemical cell. The two basic electrochemical reactions are oxidation and reduction reaction, such as:

$$Fe^{++} + 2e^{-} \rightarrow Fe$$

$$Cu^{++} + 2e^{-} \rightarrow Cu$$

$$Fe \rightarrow Fe^{++} + 2e^{-}$$

$$Cu \rightarrow Cu^{++} + 2e^{-}$$

The first two reactions are reduction that electrons are accepted by ions, and the last two are oxidation that atoms lose electrons.

Note that reduction and oxidation reaction coexist, the situation that both reactions reach a dynamic balance is called equilibrium. If the potential is below the equilibrium potential, the reduction will dominant. Consequently, the metal is stable. However, if the potential is above the equilibrium potential, the metal will be oxidized since the oxidation reaction is dominant.

The electrode is part of the electrochemical reaction that acts as an electrical conductor between the electrolyte and metal. One of the electrodes is called anode where oxidation reaction takes place while the reaction on the other electrode called cathode is reduction. The potential of electrode can be tested between electrode and the electrolyte which depends on the transfer of electrons and ions across the interface.

Since there are two electrodes in an electrochemical cell, a reference electrode should be defined for half-cell reactions. A common way to study half-cell reaction is at a standard temperature below 25° C, an effective concentration 1 mol/L, an air pressure of 1 atm, using pure species and selecting standard hydrogen electrode as a reference. The standard potential for reduction reactions are listed in Table 3.1.

In addition, there are a variety of reference electrodes used in industry listed in Table 3.2:

Table 3.1: Standard potential of some species

Electrode	Electrode reactions
Au^+/Au	+1,68
O_2/H_2O	+1,23
Pt^{++}/Pt	+1,19
Ag^+/Ag	+0,79
Fe^{+++}/Fe	+0,770
Cu^+/Cu	+0,522
Cu^{++}/Cu	+0.340
H^+/H_2	+0.00
Pb^{--}/Pb	-0.126
Sn^{--}/Sn	-0.136
Ni^{--}/Ni	-0.23
Co^{++}/Co	-0.277
Fe^{++}/Fe	-0,44
Zn^{++}/Zn	-0,763
Cr^{+++}/Cr	-0,913
Ti^{+++}/Ti	-1,630
Al^{+++}/Al	-1,66
Mg^{++}/Mg	-2,363
Na^+/Na	-2,71

Table 3.2: Electrode potential of reference electrode vs S.H.E

Reference electrode	Potential (V) vs Standard hydrogen electrode
Standard Hydrogen Electrode (SHE)	0
Saturated Calomel Electrode (SCE)	+0.241
Copper/Copper Sulfate (CSE)	+0.314
Silver Chloride Electrode (SCE)	+0.197
Mercury/Mercurous Sulfate Electrode (saturated in K_2SO_4)	+0.654

Most commonly used reference electrode are saturated calomel electrode (CSE) and silver chloride electrode (SCE) in an aqueous environment. However, when measuring structures like storage tanks, oil tubes that are buried under the earth, copper/copper sulfate ($Cu/CuSO_4$) half cell as reference electrode is preferred. Figure 3.2 shows the diagram of the copper/copper sulfate electrode, the copper is connected to the copper sulfate solution with a copper wire, the electrochemical elements in this electrode is Cu^{2+}/Cu .

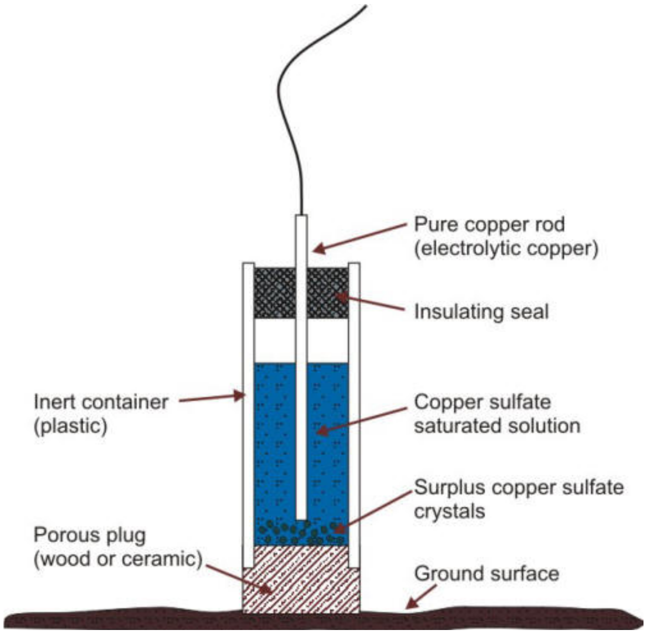

Figure 3.2: Copper/Copper sulfate reference electrode (Reprinted from [37]).

3.1.2 Butler-Volmer Equation

Nernst Equation [38] shows how the reduction potential is affected by the thermodynamic properties of the spices that involved in the chemical reaction in the electrochemical cell:

$$E_{red} = E^0 + \frac{RT}{nF} ln \frac{Ox}{Red} \tag{3.1}$$

where E^0 is the standard potential, R is universal gas constant ($8.314 J/Kmol$), F is Faraday constant ($96,585 C/mol$), n is the number of transfer electrons, T is the temperature. Ox and Red represent the thermodynamic activity of the spices.

According to Nernst equation, when the equilibrium is reached, the net exchange current i_0 is zero,

$$i_0 = i_a + i_c = 0 \tag{3.2}$$

where i_a is anodic current, i_c is cathodic current. In addition, at equilibrium according to Faraday's law:

$$k_{red} = k_{ox} = \frac{j_0}{nF} \tag{3.3}$$

j_0 is called exchange current density that the rate of both of the reactions are at equilibrium.

Consider the reaction rate constant of forward reaction and backward reaction, k_f and k_b, respectively. The net of reaction R_{net} can be:

$$\begin{aligned} R_{net} &= k_{red} C_{ox} - k_{ox} C_{red} \\ &= v_{red} - v_{ox} \end{aligned} \tag{3.4}$$

where v is the reaction rate of the redox reaction, C is the concentration of C_{ox} or C_{red} ions. The current can be defined as:

$$i = nFAv \tag{3.5}$$

where A is the surface area of the electrode.

The net current is the sum of the current of both forward and backward reaction, thus, the current can also be expressed in another form:

$$i^o = i_a - i_c = nFA(k_{red} C_{ox} - k_{ox} C_{red}) \tag{3.6}$$

Noting that the rate constant of the reaction is effected by the applied voltage E on the electrode:

$$k_{ox} = k^0 exp(\frac{-\alpha nF}{RT}\eta) \tag{3.7}$$

$$k_{red} = k^0 exp(\frac{(1-\alpha)nF}{RT}\eta) \tag{3.8}$$

where k^0 is the standard rate constant of reaction when the applied voltage E is equilibrium voltage E_{eq}, α is transfer coefficient.

By substituting Eq.(3.7) and Eq.(3.8) into Eq.(3.6), the current of reaction is:

$$i^o = nFA(k^0 exp(\frac{(1-\alpha)nF}{RT}\eta)C_{ox} - k^0 exp(\frac{-\alpha nF}{RT}\eta)C_{red}) \tag{3.9}$$

For $i_0 = nFAk^0C$, the equation will be:

$$i^o = i_0(exp(\frac{-\alpha nF}{RT}\eta) - exp(\frac{(1-\alpha)nF}{RT}\eta) \tag{3.10}$$

Eq.(3.10) is called Butler-Volmer equation which describes the relationship of current and the voltage applied to the electrode in the electrochemical cell. The current density can be expressed as:

$$j^o = j_0(exp(\frac{-\alpha nF}{RT}\eta) - exp(\frac{(1-\alpha)nF}{RT}\eta) \tag{3.11}$$

In most cases, the reverse reaction can be ignored if the over-potential is large enough, and only one direction of reaction is needed for study. Therefore, for a large enough negative over-potential, the cathodic current density can be denoted as:

$$j^o = j_0 exp(\frac{-\alpha nF}{RT}\eta) \tag{3.12}$$

For a large positive over-potential, the anodic current density is:

$$j^o = j_0 exp(\frac{(1-\alpha)nF}{RT}\eta) \tag{3.13}$$

Equation (3.12) and (3.13) are called Tafel equation.

At a room temperature of 25° C or 298.15K, Tafel equation becomes:

$$E_{red} = E^0_{red} + \frac{0.05916}{z} ln\frac{Ox}{Red} \tag{3.14}$$

Choose anodic current density for example, Tafel equation can be described as:

$$lnj = lnj_0 + \beta_\alpha \cdot \eta \tag{3.15}$$

or

$$\eta = \beta_\alpha \cdot ln\frac{j}{j_0} \tag{3.16}$$

where $\beta_\alpha{=}\frac{(1-\alpha)nF}{RT}$ is the slope, η is over potential, j is the current density, j_0 is exchange current density.

Similarly, for cathodic current density, Tafel equation becomes:

$$\eta = \beta_c \cdot ln\frac{j}{j_0} \tag{3.17}$$

where $\beta_c = -\frac{\alpha nF}{RT}$, which implies that $\beta_a + \beta_c = 1$

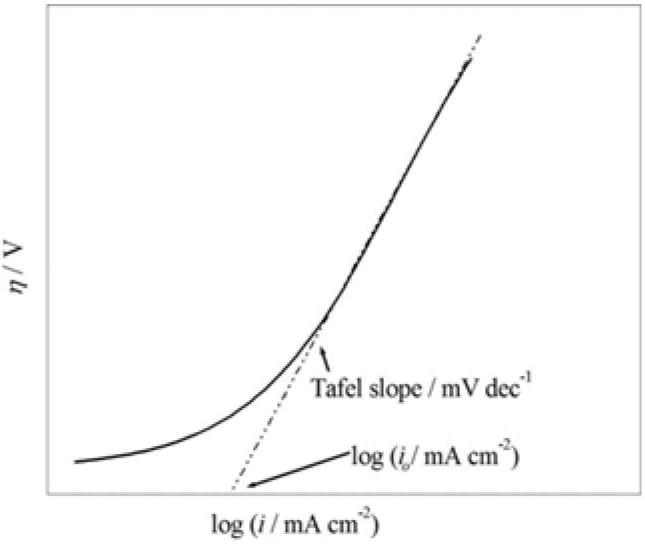

Figure 3.3: Tafel plot demonstrates the exchange current density and Tafel slope (Reprinted from [39]).

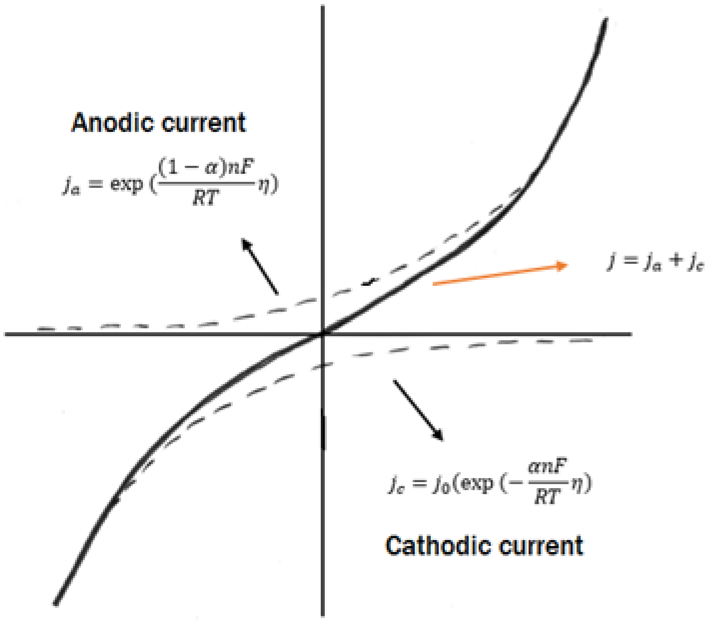

Figure 3.4: Tafel slope that shows the anodic and cathodic currents relationship.(Reprinted from [40])

Figure 3.3 shows Tafel slope in a unit of mV/dec and the exchange current density in logarithm form. Anodic current density becomes linear when over-potential is large enough. When over-potential is small, the reverse current density can't be ignored resulting in the curve both in anodic current and cathodic current as shown in Figure 3.4. Another form of Tafel equation can be derived as:

$$\eta = \frac{-RT}{2.303(1-\alpha)nF} log_{10} j_0 + \frac{RT}{2.303(1-\alpha)nF} log_{10} j \tag{3.18}$$

Among several parameters in Tafel equation and Butler-Volmer equation, charge transfer coefficients need to be tested. A conventional way is to fit an empirical equation to voltage curves [41][42]. An improved method based on integral characteristics of experimental fuel polarization curves which allows an estimation of both anodic and cathodic transfer coefficients is also provided[43]. Table 3.3 listed exchange current density of several species in 1 mol/kg, H_2SO_4

Nie's group did a research on the soil from a coast city located in north china [45], the chemical composition of the soil sample is shown in Table 3.4.

Polarization curves are fitted in order to obtain the parameters shown in Table 3.5. E_{corr} is the corrosion potential, b_a and b_c are anodic and cathodic Tafel slope,

Table 3.3: Exchange current density [44]

Metal	$I_0 (A/cm^2)$
Pt	10^{-2}
Rd, Rh	10^{-4}
Fe, Au	10^{-6}
Ni, Ag, Cu	10^{-7}
Sn, Al	10^{-10}
Zn	10^{-11}
Pb, Hg	10^{-13}

Table 3.4: Tested concentration of ions in soil [45]

NO_3^-	Cl^-	SO_4^{2-}	CO_3^{2-}	HCO_3^-	pH
0.06	1.14	0.16	0	0.02	8.8

respectively, I_{corr} is the corrosion potential.

3.2 Setting of Anodes

The requirement of current density on the surface of the protected structure can be obtained from Appendix C, and the coating efficiency or corrosion situation should be taken into consideration. The total current I_t needed can be [46]:

$$I_t = \eta \cdot i \cdot A \tag{3.19}$$

where η is the coating efficiency, i is the current density required for protection, A is the total surface area of the structure.

Due to the weather and geography conditions, soil in British Columbia is normally moisty and sticky for most of the days. The soil resistivity is about 2,000 (ohms-cm) according to Table 3.6. The surface area of the structure or device ready to be protected. Several equations are provided as the method to decide the settings for

Table 3.5: Thermodynamic parameters of tested soil [31]

$T/°C$	20	30	40	50	60	70
$E_{corr}(mV)/SCE$	-722	-711	-695	-707	-706	-694
$b_a(mv/dec)$	901	455	290	142	185	164
$b_c(mv/dec)$	96	101	116	135	142	202
$I_{corr}(\mu A/cm^2)$	15.9	16.9	28.2	32.4	54.1	69.2

Table 3.6: Corrosivity of steel buried in soil [47]

Soil resistivity (ohm-cm)	Corrosivity
0-2000	Severe
2000-10000	Mild to severe
10000-30000	Mild
30000+	Not likely

anodes. First, the number of anodes needed to satisfied manufactures limitation is[46]:

$$N = \frac{I}{A_1 I_1} \tag{3.20}$$

where A_1 is anode surface area, I_1 is recommended maximum current density output.

Number of anodes needed to meet maximum ground-bed resistance requirements are [46]:

$$N = \frac{\rho K}{L\frac{R_a - P\rho}{S}} \tag{3.21}$$

where R_a is the anode resistance, ρ is the resistivity of soil, K is anode shape factor, P is the paralleling factor, S is the center to center space between anode and backfill columns. Parameters K, P and S and can be obtained from Appendix C. The number of anodes will be decided by the maximum number of the results from Eq.(3.20) and Eq.(3.21). Substitute the number of the anodes N into Eq.(3.21) to calculate the resistance, the output voltage requirement can be calculated by Eq.(3.22), where 1.5

is a factor that takes aging of the system into consideration.

$$V_{rec} = I \cdot R_T \cdot 1.5 \tag{3.22}$$

Figure 3.5 gives two examples of anodes that are used for ICCP system including graphite and magnesium anode. Graphite anodes are chosen for the reason that they won't release toxic as stainless steel or decay as fast as aluminum [48], while having a good electric conductivity. Magnesium anodes can be popular for its negative properties among lots of metals while eliminating the extreme expensive negative metals, such as gold. Apart from these two types, polymer anodes such as carbon fiber reinforced polymer anode shows a balanced performance both electrically and mechanically with a service life of 12 years [49]. Carbon fiber reinforced polymer also be proved the ability to strengthen the corroded RC beam and sustain a high current density [50].

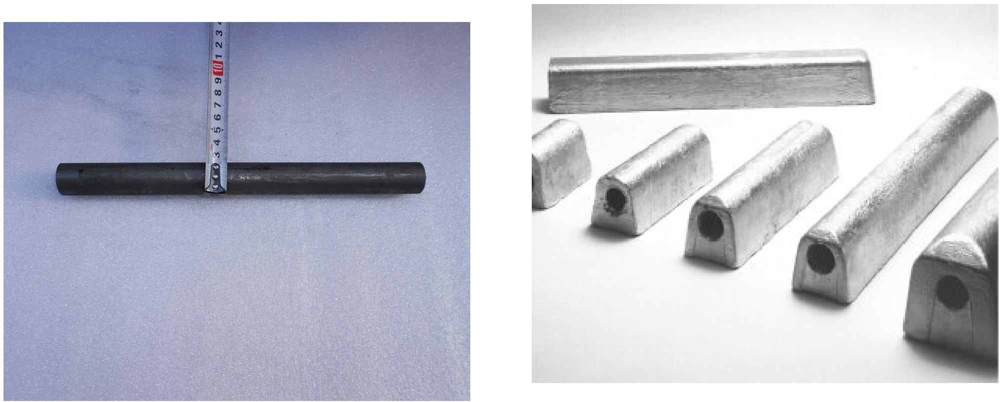

(a) Graphite anode (Reprinted from [51])

(b) Magnesium anodes (Reprinted from [52])

Figure 3.5: Anodes that used for corrosion protection in sacrificial anode system or impressed current corrosion protection system.

Chapter 4

Implementation Methods

The simulation for the model of the energy harvester and ICCP of cathodic corrosion protection can be achieved by COMSOL Multiphysics, in this chapter the methods for building models, settings for simulation will be introduced step by step.

4.1 Building geometry by SolidWorks

The geometry function in COMSOL provides tools that are enough to draw 2D model, when it comes to a 3D complicated geometry, CAD software is much more operable than COMSOL. SolidWorks gives solution for 3D design, simulation, electrical design, data management and so on, which is chosen for building a 3D steel structure for corrosion protection simulation in COMSOL. The geometry or mesh result in SolidWorks can be imported into COMSOL for further study. To build a structure as shown in Figure 4.1, the following steps should be done:

1. Locate the 'top plane' as the work plane, right click the 'top plane' to open a 3D sketch. Then draw the basic line of the structure.

2. To make the lines become a 3D structure, build a 'structure member' from 'insert', 'weldment', for chosen lines. There are several kinds of structure member that are based on standards all over the world.

3. However, the structure member provided are all hollow, it would be problematic when it is removed from the whole model to obtain the interface of the structure in COMSOL. Therefore, a customized 'structure member' can be created and save it in the default structure member library path for choosing.

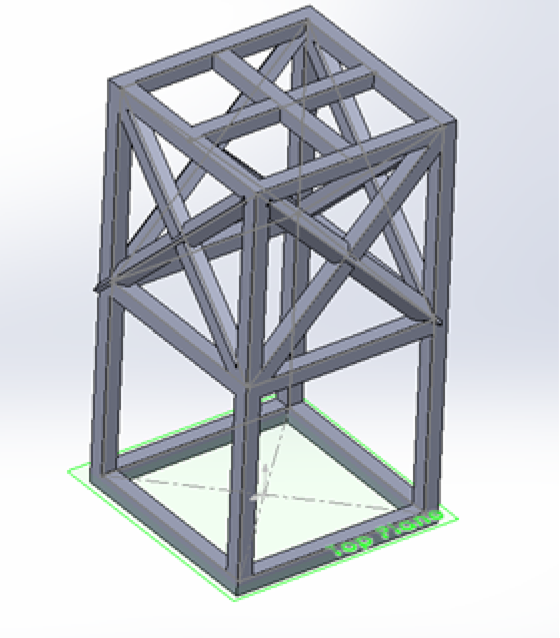

Figure 4.1: Steel structure that is 2-meters height and 1-meter width built by SolidWorks.

4. Combine the whole structure after setting the structure member and trim the sharp boundaries of the structure.

For the steps of building the 3D structure for energy harvester in SolidWorks, the steps are shown in Appendix D, while the 2D-axisymmetric model for energy harvester can be directly built in COMSOL.

4.2 Simulation Energy Harvester in COMSOL Multiphysics

COMSOL Multiphysics provides various kinds of modules that can be used for simulating complicated multi-physics models.

There are seven basic steps for simulating in COMSOL:

1. A 'model wizard' can help choose a specify model including 3D, 2D, 2D-axisymmetric, 1D-axisymmetric, 1D and 0D. The energy harvester can be built as 3D model or a 2D-axisymmetric model under a 'Magnetic and Electric Fields'(mef) from 'AC/DC' module, 'mef' can be used to solve situation contains excitation sources such as current or voltage, and then produce results which will be

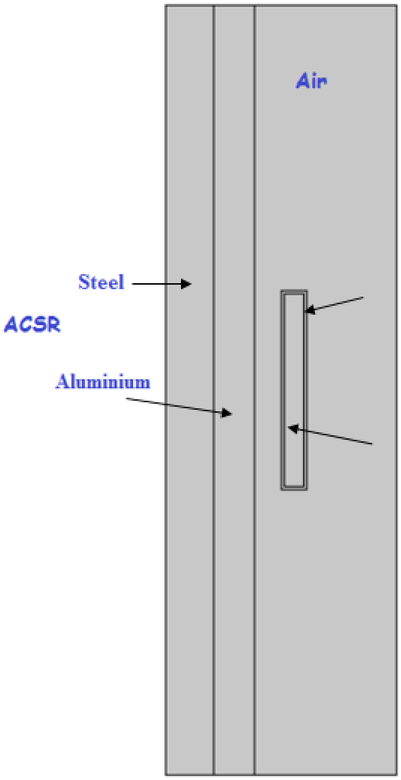

Figure 4.2: The geometry structure of 2D-axisymmetric model for energy harvester including air, ACSR conductor, coil and the magnetic core.

explained in the post processing part.

The AC source exists in the high voltage transmission line, the frequency domain for the study is chosen since it can compute the response of a given input harmonic excitation for a certain frequency.

2. COMSOL provides tools to built diversified geometry. Geometry can also be imported into COMSOL simply by the import function from the geometry section located in 'Home' toolbar.

   Benefiting from this feature, geometry files created by AutoCAD, SolidWorks, SolidEdge and can be directly imported to COMSOL and recognized as solid. For 3D structure created in SolidWorks, magnetic core, coils, and conductor should be covered by an air block as the practical environment. For 2D-axisymmetric version energy harvester model, COMSOL geometry tool is enough to draw the geometry as shown in Figure 4.2. The ACSR conductor can be simplified into a concentric cylinder model shown in Figure 4.3.

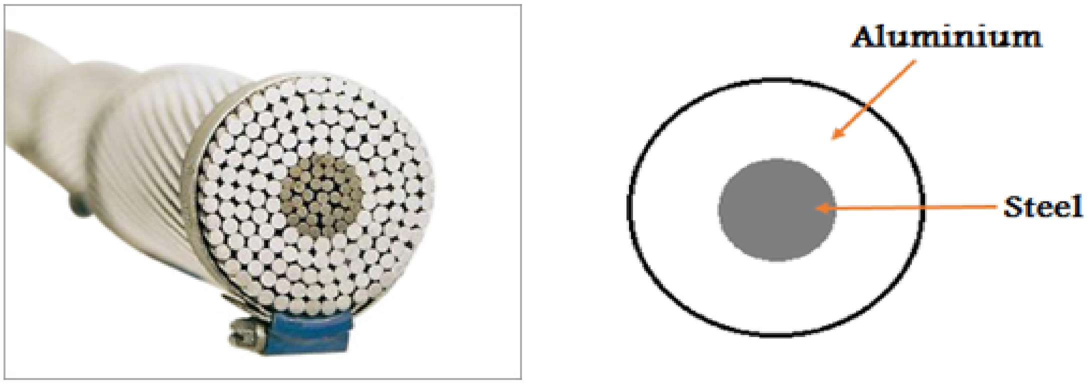

(a) ACSR conductor (Reprinted form [53]) (b) Simplified ACSR conductor cross-section

Figure 4.3: Cross-section of ACSR conductor.

However, the 2D-axisymmetric model is limited by the dimensions making the core gap impossible to be modelled. The problem can be solved by replacing the relative permeability of magnetic core into effective permeability that takes the fringing flux effect caused by core gap into consideration.

3. Add material from 'Material' button on the 'Home' toolbar, then the material library is displayed. Choosing nickel steel Mu-metal 80 percent Ni for the core, aluminum for the conductor, copper for the coil and air for the rest part of the model.
   The properties of copper coil are varied by the type of AWG, here AWG20 is chosen for simulation, properties of AWG are listed in Table 4.1, that are defined at room temperature, DC or AC that lower than or equal to 60Hz.

Table 4.1: Properties of AWG20 [54]

Diameters	Cross section Area	Resistance
0.032 inch or 0.812 mm	0.518mm^2	33.31Ω/km

4. On the physics toolbar, one can define the physic conditions by domain, boundary, edges, and points. After creating the magnetic field and electrical field model, some default settings for the model automatically includes magnetic insulation of the exterior surface, ampere's law that covered the whole model. The excitation source of the magnetic induction energy harvester is AC. For the

frequency of the current, it can be defined in the study section. The input of the conductor can be set by creating a new 'magnetic insulation' that contains only the conductor terminal domains. Select 'Terminal' and 'Ground' for each terminal.

To set the coil domain, create a new physics 'Magnetic Field', and select 'Single turn coil' for the coil domain with no excitation source. Then add 'Gauge Fixing for A-field' for 'mef'.

In the setting windows for 'mef', select 'In-plane vector potential' in components. And select 'Out-plane vector potential' for 'mf '.

5. The geometry will further be divided into sub-domains for the need to convert the geometry entity into discretized numerical entity. Therefore the process can be operated numerically.

6. COMSOL provides several solvers for computing the program including MUMPS, PARDISO, and SPOOLES. All the three solvers will help solve finite element problems and provide same results [55], here PARDISO solver is chosen for its advantage in speed and the ability to make use of 'out of core' function to reduce the requirement for RAM.

   Set the frequency 60Hz and compute, the information for the model can be checked from log window.

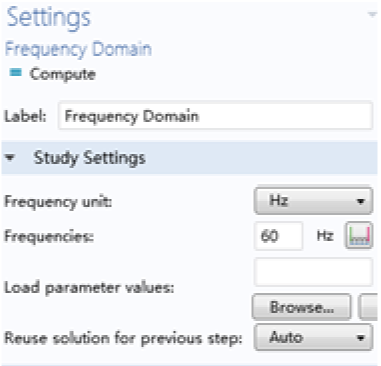

Label: Frequency Domain

Frequency unit: Hz

Frequencies: 60 Hz

Load parameter values:

Reuse solution for previous step: Auto

Figure 4.4: Window for setting the frequency domain for energy harvester simulation.

7. After running the simulation successfully, a set of data results is obtained for the model. Right click the 'Result' and choose '2D plot group' which will create a blank expression for plot the model on 2D surface, thus, choose 'inductive current density r-direction' or 'inductive current density z direction', the final

result of inductive current density in the coil will be plotted on the right hand window.

4.3 Simulation ICCP in COMSOL Multiphysics

1. Setting up the model for impressed current cathodic protection model requires the electrochemistry module, 'Secondary current distribution' is chosen for it can measure the situation that over potential is important, the relation between over potential and charge transfer can be expressed by Butler-Volmer equation and Tafel equation which is introduced in Chapter 3.

   Before go on to the next step, the basic idea of current distribution in electrochemistry model in COMSOL should be clear. As in an electrochemical cell, current density and potential are to be solved in both electrode and electrolyte, thus, assume a metallic conductor that is chosen as electrode, the relation between current density and voltage will be:

   $$i_s = -\sigma_s \nabla \phi_s \tag{4.1}$$

   Equation (4.1) is derived from ohm's law, where $i_s(A/m^2)$ is the current density vector in the electrode, $\sigma_s(S/m)$ is the conductivity in the electrode, ϕ_s is the electric potential.

   Similarly, in the electrolyte, derived from ohms law:

   $$i_l = -\sigma_l \nabla \phi_l \tag{4.2}$$

   where $i_l(A/m^2)$ is the current density vector in the electrolyte, σ_l is the conductivity of the electrolyte, ϕ_l is the electric potential.

   At the interface, the over potential of the cell is $\eta = E - E_{eq}$ and can be described as the form of electric potential:

   $$\eta = \phi_s - \phi_l - E_{eq} \tag{4.3}$$

   Based on Butler-Volmer equation, the current density can be expressed as a function of charge transfer coefficient, temperature, exchange current density and over potential:

$$j_{loc} = j_0(exp(\frac{\alpha_a nF\eta}{RT}) - exp(\frac{-\alpha_c nF\eta}{RT})) \tag{4.4}$$

where j_{loc} is the local current density, j_0 is the exchange current density, β_a and β_c is the anodic and cathodic charge transfer coefficient, respectively.

2. The geometry of the structure is created by SolidWorks and imported into COMSOL which steps are similar to energy harvester model. In addition, a surrounding electrolyte should be created for covering the structure. Thus, a cylinder is simply created by COMSOL as the electrolyte. However, the electrolyte will be finite as it is limited in a cylinder, by applying 'infinite element' function on the exterior boundaries of the cylinder, the electrolyte becomes infinite.

   As in the corrosion model, the interface of electrode and electrolyte is the element for measuring. The geometry imported from SolidWorks is solid, it should be processed to be hollow, thus, the 'difference' function in 'Boolean and partitions' button from geometry toolbar is used to remove the structure from the whole model. The final geometry results for the further process are the electrolyte, the interfaces of the anodes and protected structure, since the interface between electrolyte and electrode is the one need to be analyzed. Figure 4.5 illustrates the corrosion model including the structure and the electrolyte.

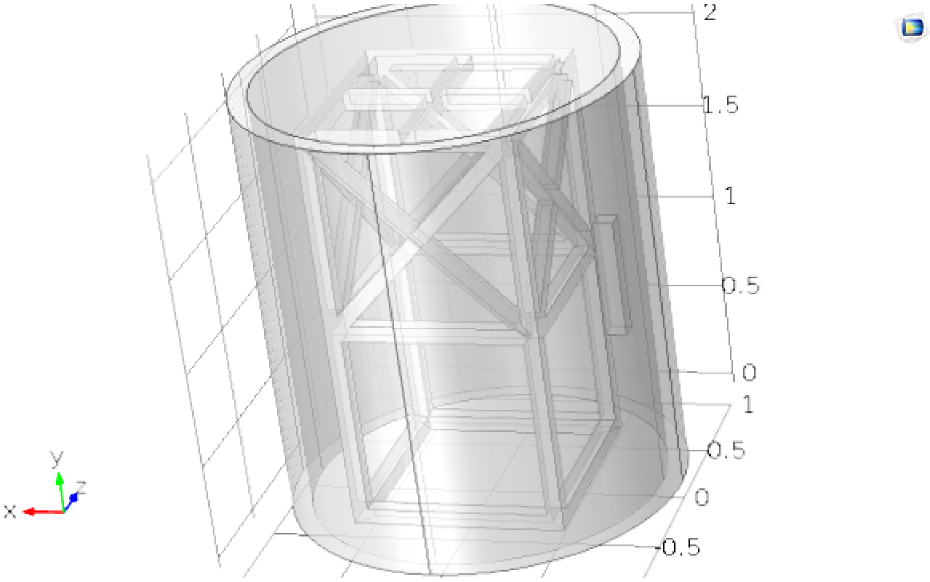

Figure 4.5: Imported geometry structure for ICCP including steel structure, anode and electrolyte.

Table 4.2: Parameters defined in Definition toolbar

Parameters	Value
Soil resistivity	0.05 S/m
Exchange current density	$10^{-6} A/m^2$
Impressed current	Calculate in chapter 6
Cathodic tafel slope	96 mV/dec

3. (a) Choose the electrolyte domain of the model, locate the ‘Electrolyte 1’ section, set the electrolyte conductivity as ‘user defined’, type ‘sigma’ in the next blank.

   (b) Locate ‘Initial Values 1’ and type ‘0.5’ in the electrolyte potential for initial setting.

   (c) Locate the ‘Electrolyte Electrode Boundary Interface 1’ and set the external electric potential in boundary condition section 0 V.

   (d) In the sub path of ‘Electrolyte-Electrode Boundary Interface 1’, the ‘Electrode Reaction 1’ is used to set kinetic parameters for the electrochemical

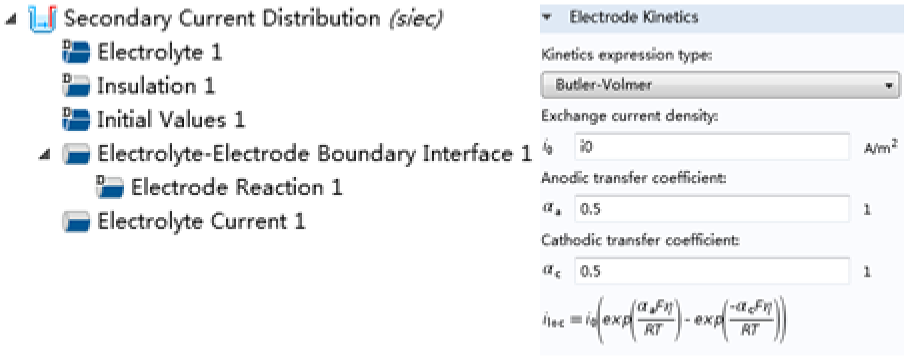

Kinetics expression type: Butler-Volmer

Exchange current density: i_0 i0 A/m^2

Anodic transfer coefficient: α_a 0.5 1

Cathodic transfer coefficient: α_c 0.5 1

$$i_{loc} = i_0\left(exp\left(\frac{\alpha_a F\eta}{RT}\right) - exp\left(\frac{-\alpha_c F\eta}{RT}\right)\right)$$

Figure 4.6: Interface window for setting the physics parameters.

cell. Locate the 'Electrode Kinetics' section, choose 'Butler-Volmer' as the kinetics expression type and then type in the parameters as exchange current density, anodic transfer coefficient, cathodic transfer coefficient.

(e) Locate the 'Electrolyte current 1' section for typing the current that will be add on the electrodes generated from rectifier.

4. Click 'Build All' in 'Mesh 1' and mesh the whole model.

5. After finishing the mesh, run the study directly.

6. The cathode part of the results can be shown by 'selection' function that selects only cathode domains of results and plots them. The 1D potential distribution can be plotted by selecting a certain edge of the steel structure with '1D plot'. All the results will be displayed in Chapter 6. The computer used for simulation of 2D axisymmetric energy harvester model and ICCP model has 1.7 GHz Intel Core i5, 4 GB 1333MHz DDR3 RAM.

Chapter 5

Analysis of Simulation Results of Energy Harvester

In this chapter, results of output induced voltage is calculated by MATLAB, COMSOL and LTspice.

5.1 Output Induced Voltage of Energy Harvester

Based on Eq.(2.4), the induced voltage can be calculated when several parameters such as core width (d), core length (w), number of turns of the coil (N), the inner and outer distance of the core D_i and D_0 are defined respectively and the root mean square value of current flowing through the conductor are calculated. When the core gap is 1 mm, the effective permeability μ_e is derived, and the relation between N and induced voltage (V) can be computed. As a comparison, the energy harvester is also simulated in COMSOL to obtain a numerical solution, the simulation results of magnetic flux density are shown in Figure 5.1 (2D-axisymmetric) and Figure 5.2 (3D), and the induced current density (A/m^2) is shown in Figure 5.3. In Figure 5.1 and 5.2, a 50 mm height, 5 mm width, 71.6 mm outer diameter and 61.6 mm inner diameter magnetic core winded by coils is placed on a simplified ACSR conductor, the distance between the conductor and the outer edge of the coil is 7 mm. The magnetic flux density decreases as the distance away from the conductor becomes larger. In Figure 5.3, the induced current density on z-axis is plotted, the intensity of the current density shows opposite sign which indicates opposite current flow directions that forms a circuit, the slight difference between the maximum intensity of both sides current density is caused by the different distances away from the conductor. As shown in Figure 5.2, the 2D model does not include core gap while in practice such core gap will lead to a considerable reluctance. To take this effect into account, the effective permeability about 361 for Mu-metal (calculated from Eq.(2.6)) should be applied in COMSOL.

Then the induced voltage is calculated by $V_{in} = j_{in} \cdot A \cdot Z$, where j_{in} is the induced current density, A is the cross-section area of the coil, Z is the impedance of the coil, and then compared with the ideal case, the results are illustrated in Figure 5.4. The main reason that the result of COMSOL simulation is much smaller than the ideal case is caused by loss of heat from the coil and magnetic core. In the ideal case, the conductor is an ideal wire, while in the COMSOL, a simplified ACSR conductor is applied in COMSOL which contributes much loss in aluminum and steel making the current flow through the conductor much smaller.

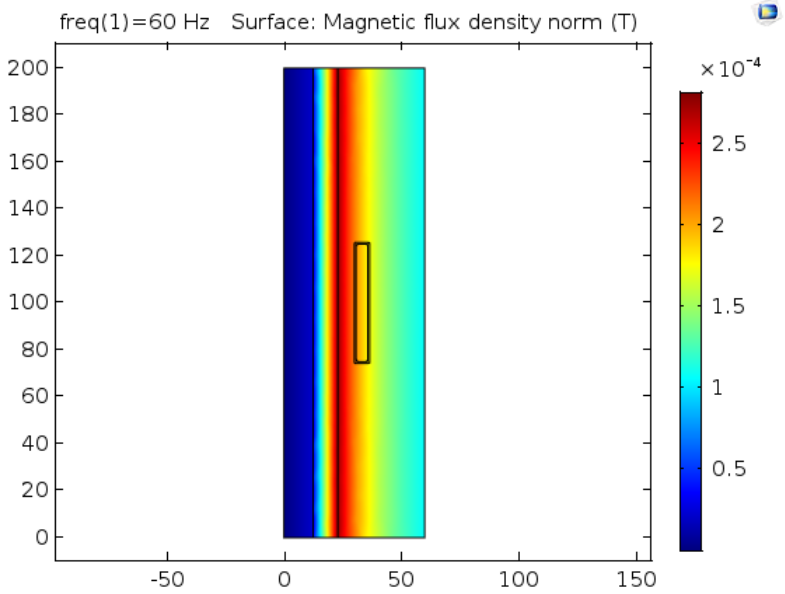

Figure 5.1: The magnetic flux density (T).

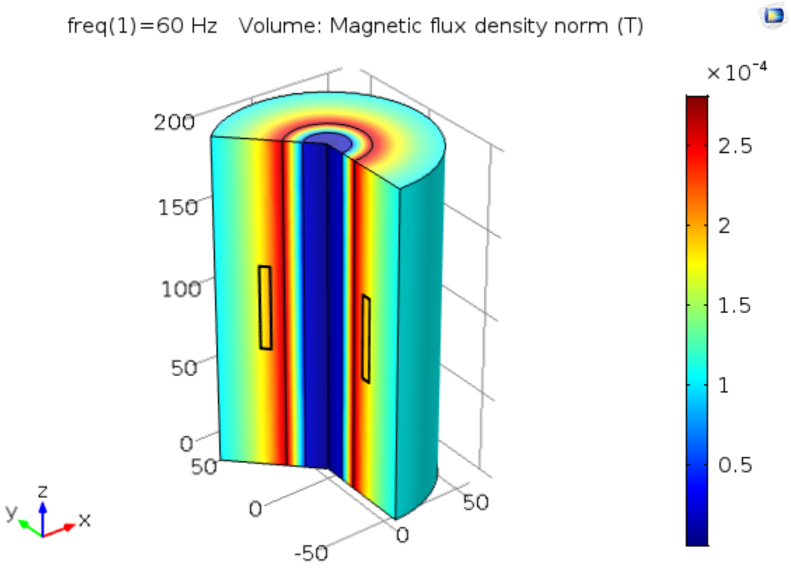

Figure 5.2: 3D plot of magnetic flux density (T).

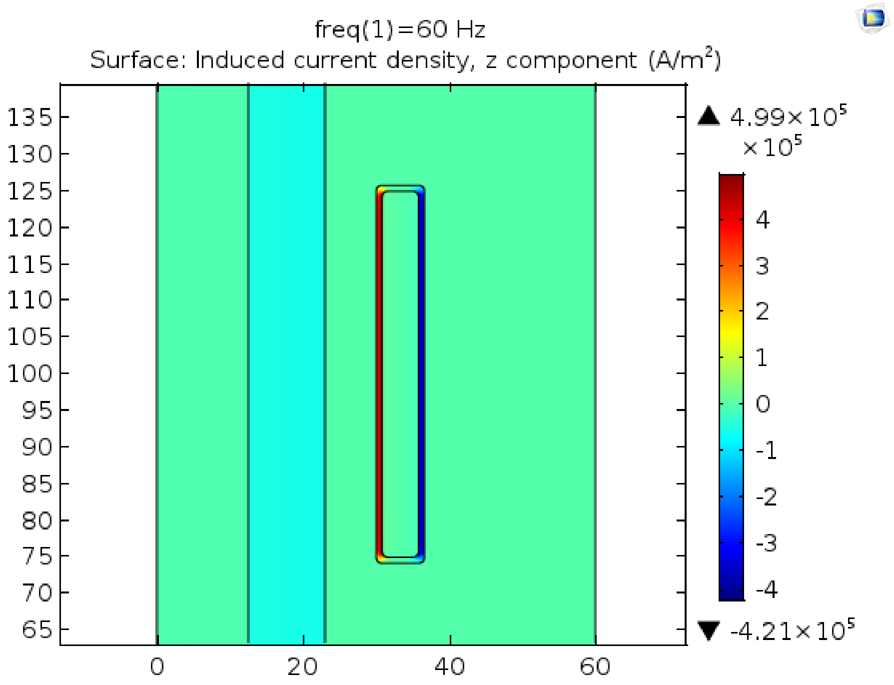

Figure 5.3: Induced current density in the coil.

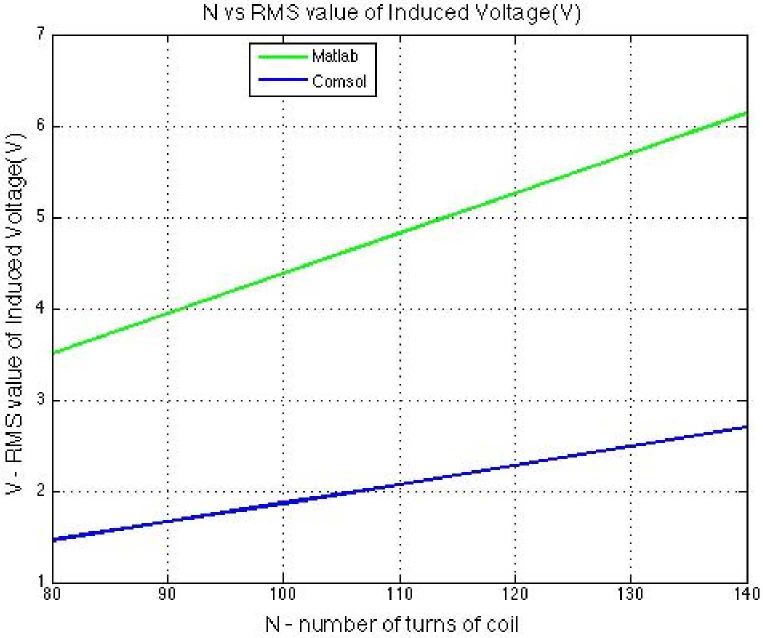

Figure 5.4: The induced voltage generated in the coil vs the number of turns of coil (N). (Core width (d) is 5mm, core length (w) is 50mm, I = 65A.)

After zoom in the inductive current density with both r-axis and z-axis as illustrated in Figure 5.5, it is noticed that the current density at the corners of the coil is much more higher than the other part.

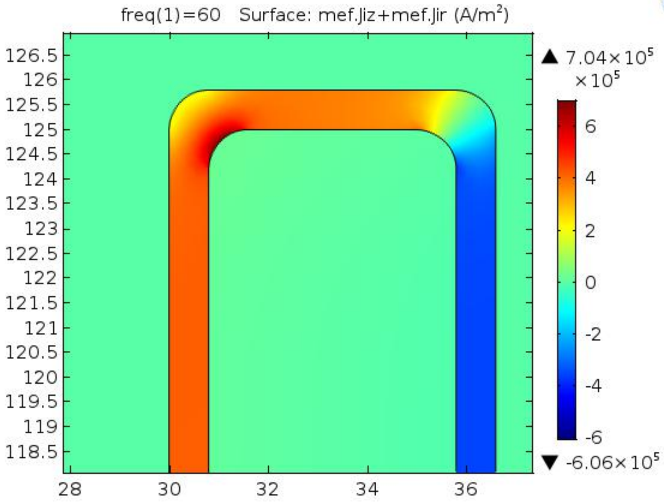

Figure 5.5: Zoom in view of induced current density in the coil

5.2 Rectification Result of DC Output Voltage

According to Appendix B, the supply input voltage for the chosen temperature sensors is 2.5V-5.5V, split-capacitor and voltage doubler with active diode are tested in LTspice with input 2.694V AC source with N=140 is chosen, parameters of energy harvester are listed in Table 5.1.

Table 5.1: Parameters of energy harvester for supplying sensors

Parameters	Value
W (core length)	50mm
D (core width)	5mm
N (number turns of coil)	140
D_o (outer diameter)	71.6mm
D_i (inner diameter)	61.6mm

The simulation result of output voltage of split capacitor and voltage doubler with active diode with 2.694V input and 1k Ω load resistor is shown in Figure 5.6 and Figure 5.7. It takes about 0.8s to achieve an output 3.6V for a split capacitor, the output of voltage doubler with active diode can be roughly 4V since positive output is about 2V and negative output is about 2V, both of the output are stable and enough for supplying temperature sensors according to Appendix B.

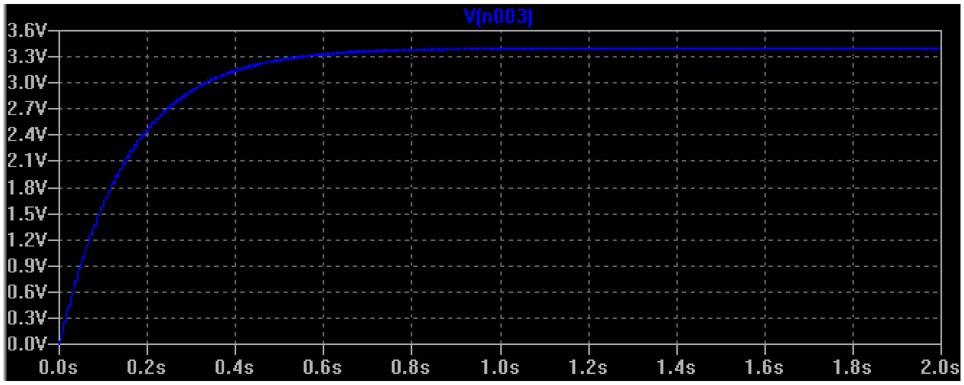

Figure 5.6: Output voltage of split capacitor for 2.694V input, 1k Ω load resistor.

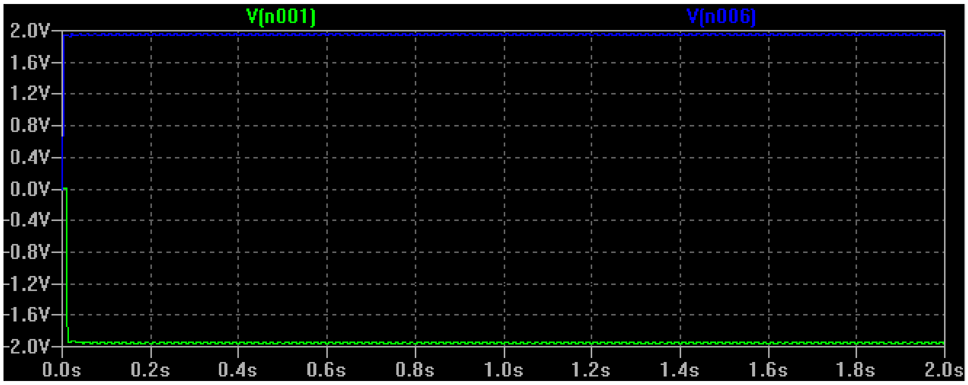

Figure 5.7: Output voltage of voltage doubler with active diode for 2.694V input, 1k Ω load resistor.

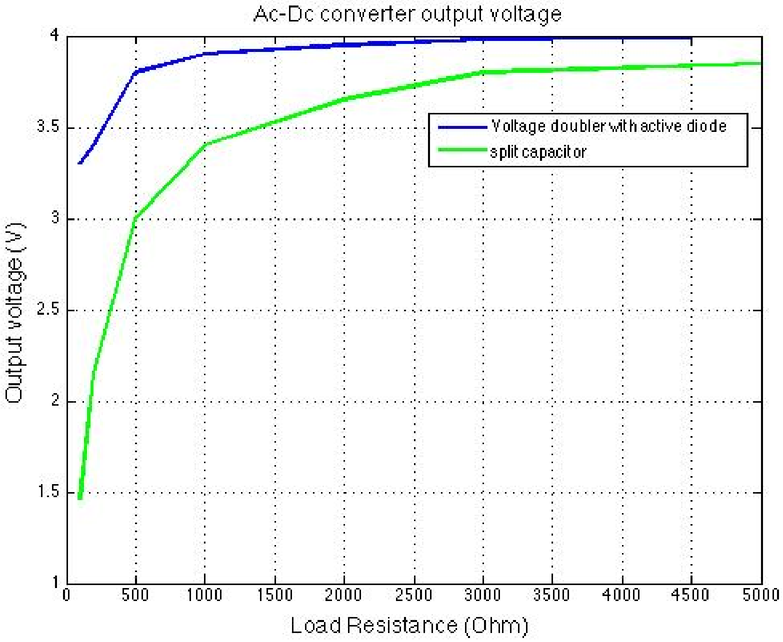

Figure 5.8: Output voltage of split-capacitor and voltage doubler with active diode vs. Resistance of the load.

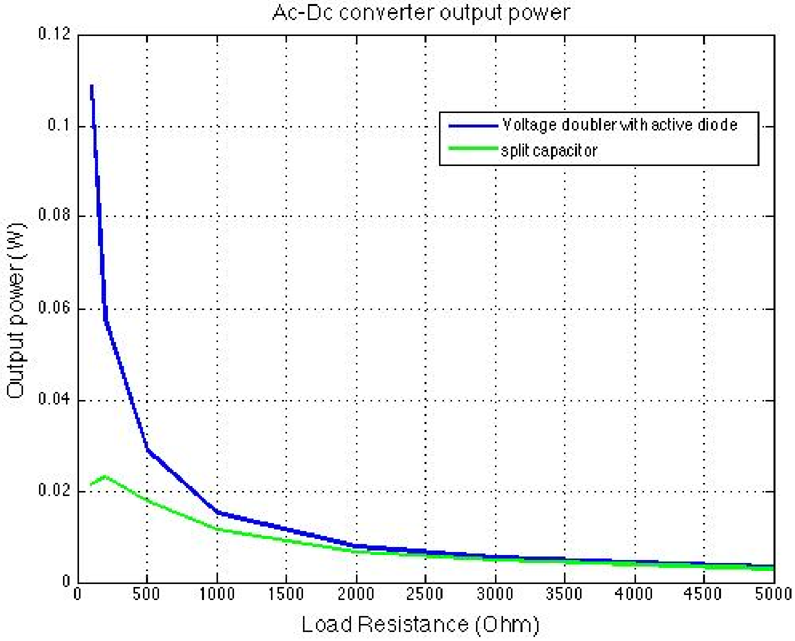

Figure 5.9: Output power of split-capacitor and voltage doubler with active diode vs. Resistance of the load.

From Figure 5.8 and Figure 5.9, the output voltage of voltage doubler with active diode is much larger than that of split capacitor until the resistance of load is as much as 4.5k Ω. When it comes to a low resistance load (under 500 Ω), the output wave of voltage doubler fluctuates much more than that of split capacitor as illustrated in Figure 5.10, even though the output voltage is much higher, split capacitor can be stable for application.

For powering low resistance load devices, increasing the number of turns of coil, the width and height of the core can make the device to generate sufficient output voltage of split capacitor enough for supply voltage and avoid the fluctuation. When the device is loaded with resistance over 1kΩ, both of the AC-DC converters are suitable as long as output voltage is high enough.

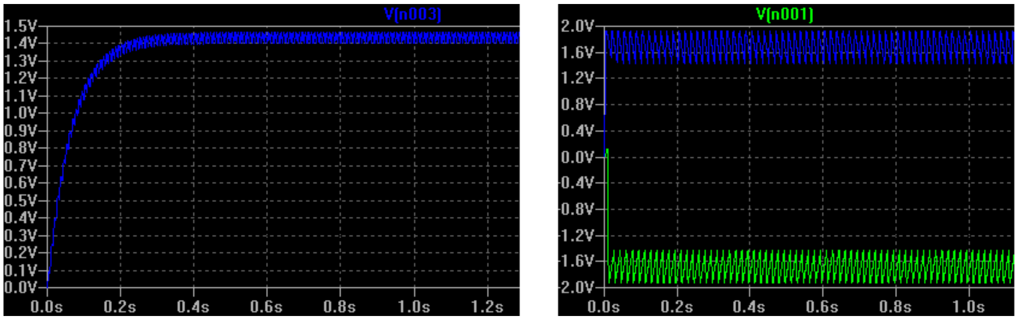

Figure 5.10: Output voltage of split capacitor (left) and voltage doubler with active diode (right) for 2.694V input, 100 Ω load resistor.

Chapter 6

Analysis for ICCP Simulation Results

The induced current from energy harvester can also drive the protective current for corrosion prevention. In this Chapter, the simulation results of ICCP in COMSOL that illustrate the distribution of potential and local current density of the surface of the cathode is provided.

6.1 Simulation result for ICCP

For the structure built in Chapter 4.1, the requirement for impressed current can be calculated by Eq.(3.19) when the surface area of the structure is known. Assume the structure is not coated, the impressed current density needed for protection can be obtained from Appendix C, i_r=1.5mA/ft^2:

$$I_t = \eta \cdot i_r \cdot A = 1.5mA/ft^2 \cdot 5.45m^2 = 0.088A \tag{6.1}$$

The number of anodes that satisfy the manufactures' requirement can be calculated from Eq.(3.20). Based on Eq.(3.21), the number of anodes that meet the ground bed resistance requirements are:

$$N = \frac{I}{A_1 I_1} N = \rho \frac{K}{L(R_a - \frac{\rho P}{S})} < 1 \tag{6.2}$$

Thus, the total number of anodes needed for the created steel structure is one for 2.8 ft^2 surface area anode.

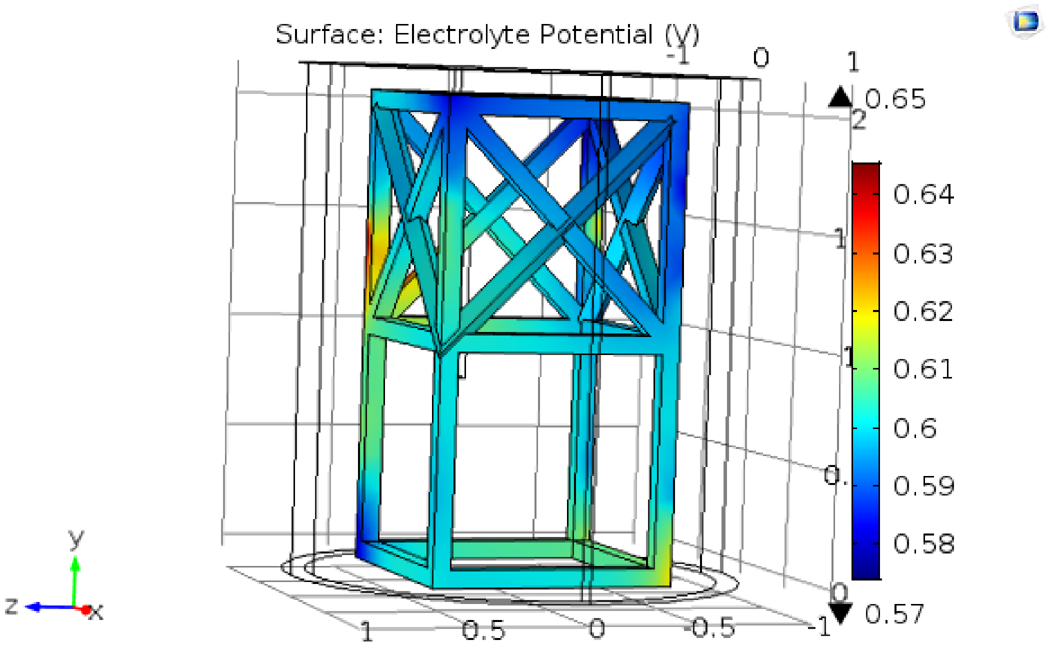

Figure 6.1: Potential vs copper/copper sulfate electrode on the surface of the cathode.

Since the voltage produced for powering the sensors is not suitable to support the corrosion protection system, the parameters for the energy harvester is re-designed and the result can be simulated in COMSOL and PSpice. The output voltage should reach the value calculated from Eq.(3.22). The calculation for parameters of energy harvester for ICCP won't be introduced since the steps are the same as for powering sensors.

Figure 6.1 shows the ICCP result of potential vs. copper/copper sulfate electrode on the interface between the structure and electrolyte, which ranges from 0.57 to 0.65V. This is a relatively low uniform potential that prevents corrosion on the steel structure.

Figure 6.2 plots the potential at one edge of the structure that is close to the anode on y-axis. The potential ranges from 0.58V-0.645V.

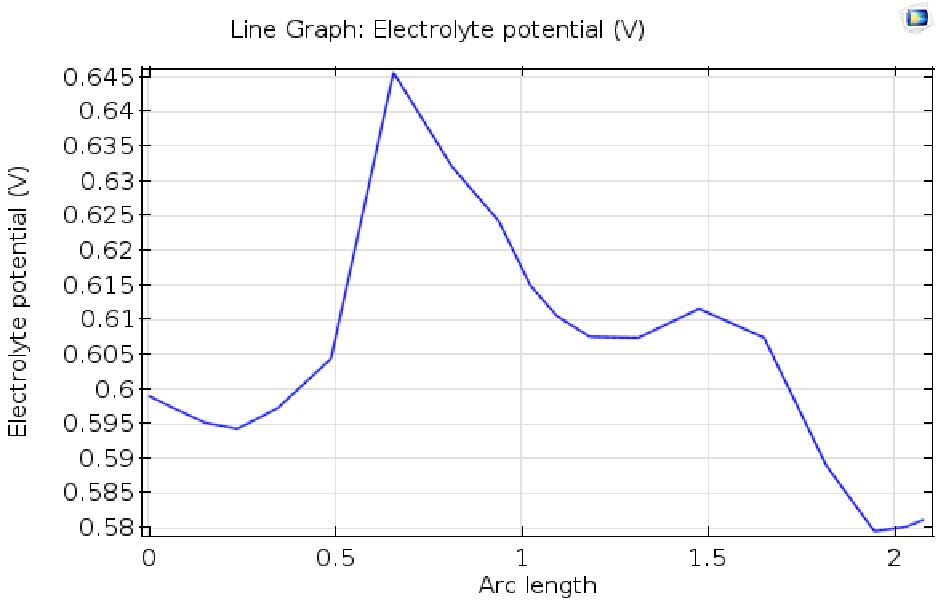

Figure 6.2: 1D plot of an edge potential on the structure near the anode.

Figure 6.3 illustrates the local current density on the surface of the steel structure ranging from -0.4 mA/m^2 to -2.06mA/m^2. The model shows a negative value of local current density that is a sum of both corrosion current density and the impressed current density, noting that the corrosion current is coming from the structure to the electrolyte which is positive. Therefore, the corrosion is prevented in this case.

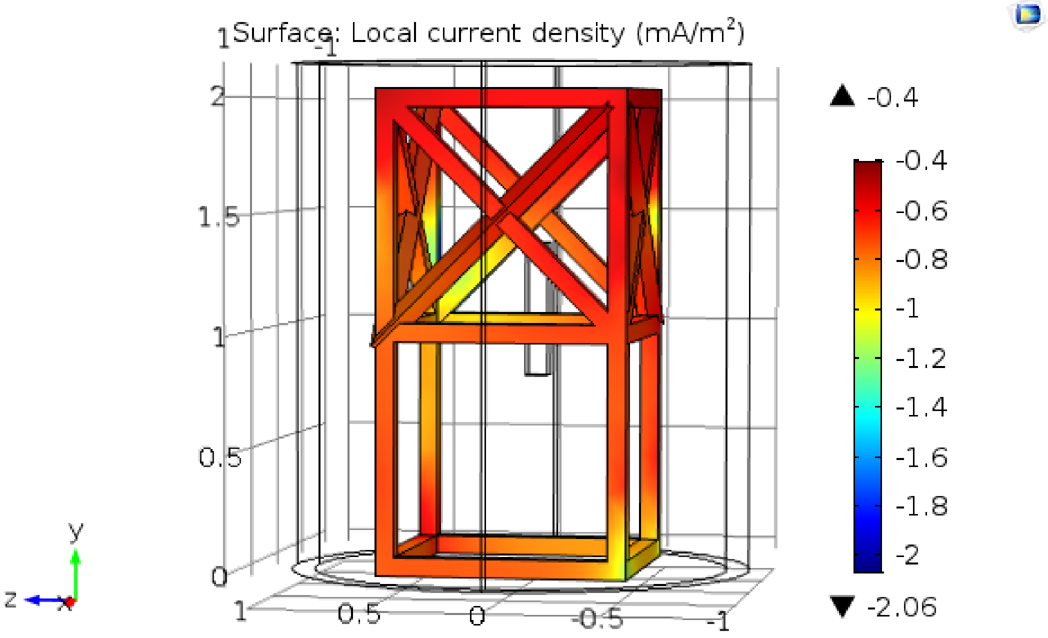

Figure 6.3: Local current density of the structure surface.

Chapter 7

Conclusion and Future Work

7.1 Summarization

A magnetic induction based energy harvester is developed for collecting the energy from high voltage transmission conductor. By applying formulas of the effective permeability of the magnetic core includes core gap, the induced voltage at the terminals of the coil can be calculated based on Faraday's law, while the induced current can be expressed by applying AC circuit theory. Two AC-DC converters are tested given the AC induced voltage input, voltage doubler with active diode works better with resistor below about 4,500 Ω, split capacitor can be much more stable when load resistance is under 500 Ω. In addition, steel structure located in the power grid can be protected from corrosion by impressed current powered from the energy harvester. The principle of electrochemical cell is studied through Butler-Volmer equation that illustrates the thermodynamics of ions and electrons both in electrode and electrolyte. After the methods of computing parameters needed for impressed current corrosion protection system is obtained, the number of anodes can be determined as well [47]. To verify the solution, numerical simulation is implemented, by building geometry for both the energy harvester and corrosion protection model in SolidWorks, COMSOL can add multi-physics environments to the imported geometry.

In summary, the energy harvester designed in this thesis can be an effective tool for collecting energy created by magnetic induction with an acceptable efficiency since the strong AC going through the conductor, the high permeability magnetic core material and the choosing of converter while supporting the impressed current corrosion protection system for steel tower.

7.2 Future Work

Although the 2D-axisymmetric model is built and ran for simulating the energy harvester successfully, the 3D model is simulated with failure because of the shortage of the computer even though the model is parted into $\frac{1}{32}$. Therefore, an optimization method should be established to make the program run smoothly.

The soil can be sampled directly from different areas in BC and studied the resistivity, Tafel slope, since the offshore area is much different from inland, the difference should be considered which will affect the design of energy harvester.

Bibliography

[1] Naser Khosro Pour. Fully integrated solar energy harvester and sensor interface circuits for energy-efficient wireless sensing applications. *Journal of low power electronics and applications*, 3(1):9–26, 2013.

[2] Y. Wen J. Zhang A. Yang C. Lu J. Yang J. Wen J. Qiu Y. Zhu Wei He, Ping Li and M. Yu. Piezoelectric energy harvester scavenging ac magnetic field energy from electric power lines. *Sensors and Actuators A: Physical*, 193(0):59–68, 2013.

[3] Ashwin A. Seshia Yu Jia. An auto-parametrically excited vibration energy harvester. *Sensors and Actuators A: Physical*, 220:69–75, 2014.

[4] L N Cattafesta III S B Horowitz, M Sheplak and T Nishida. A mems acoustic energy harvester. *Journal of micromechanics and microengineering*, 19(9), 2006.

[5] S. Monfray O. Puscasu T.Sktnicki S Boisseau, G. Depesse. Semi-flexible bimetal-based thermal enery harvesters. *Smart Market Struct*, 2, 2013.

[6] Yixin Zhou Jing Liu Guodong Xu, Yang Yang. Wearable thermal energy harvester powered by human foot. *Front. Energy*, 7(1):26–38.

[7] Solar energy power generation. `"http://www.electronicshub.org/solar-energy-power-generation/"`.

[8] Maria Bernadete de Morais França Elnatan Chagas Ferreira Andreu Cabot Pedro Carvalhaes Dias, Flávio José Oliveira Morais and José A. Siqueira Dias. Autonomous multisensor system powered by a solar thermoelectric energy harvester with ultralow-power management circuit. *IEEE TRANSACTIONS ON INSTRUMENTATION AND MEASUREMENT*, 64(11), 2015.

[9] Yaowen Yang* and Lihua Tang. Pequivalent circuit modeling of piezoelectric energy harvesters. *JOURNAL OF INTELLIGENT MATERIAL SYSTEMS AND STRUCTURES*, 20, 2009.

[10] Jeong-Ho Lee SeKwon Oh Kwi-Il Park Myunghwan Byun Hyelim Park Gun Ahn Chang Kyu Jeong Kwangsoo No HyukSang Kwon Sang-Goo Lee Boyoung Joung Keon Jae Lee Geon-Tae Hwang, Hyewon Park. Self-powered cardiac pacemaker enabled by flexible single crystalline pmn-pt piezoelectric energy harvester. *Advanced materials*, 26(28):4880–4887, 2014.

[11] Yu-Yin Chen Dejan Vasic, * and François Costa. Self-powered piezoelectric energy harvester for bicycle. *Journal of Mechanical Science and Technology*, 28(7), 2014.

[12] K. Kecik and M. Borowiec. An autoparametric energy harvester. *Eur. Phys. J. Special Topics*, 222:1597–1605.

[13] O. Aldraihem and A. Baz. Energy harvester with a dynamic magnifier. *Journl of Intelligent Material Systems and structures*, 22, 2011.

[14] Alex A. Elvin Niell G. Elvin a, n. An experimentally validated electromagnetic energy harvester. *Journal of Sound and Vibration*, 330:23142324, 2011.

[15] G2MT laboratories. Cost of corrosion in the us over 1 trilion dollars. `"http://www.g2mtlabs.com/corrosion/cost-of-corrosion/"`.

[16] Sacrificial anodes used to prevent corrosion and cathodic protection. `"http://enroutematch.com/2014/06/sacrificial-anodes-used-to-prevent-corrosion-and-cathodic-protection/"`.

[17] Background of co2 corrosion. `"https://co2corrosionchem409.wikispaces.com/Background+of+CO2+Corrosion"`.

[18] Zinc enriched2 primer. `"https://lodoffroad.com/information"`.

[19] José Maurílio da Silva and João Nelson Hoffmann. Cathodic protection for tower foundation using induction from the transmission line electric field. *IEEE*, 1, 2001.

[20] Ozan K. Electromechanical energy conversion-i. `"https://ozank.gitbooks.io/ee361/content/magnetic_circuits/README.html"`.

[21] F.Fioeillo. Measurement and characterization of magnetic materials. *New York: Elsevier*, 2004.

[22] E.C. Snelling. *Soft Ferrites/Properties and Applications.* 1969.

[23] Classes of magnetic materials. `"http://nptel.ac.in/courses/115103039/module1/lec1/5.html"`.

[24] David Jiles. Introduction to magnetism and magnetic materials. *IEEE*, 1, 1998.

[25] Magnatic Shield Corp.

[26] Nickel iron alloys telcon. `"http://shpat.com/docs/elfa/04889101.pdf"`.

[27] Wikipedia, rectifier. `"https://en.wikipedia.org/wiki/Rectifier"`.

[28] Full wave rectifier. `"http://www.electronics-tutorials.ws/diode/diode_6.html"`.

[29] Ortmanns M Peters C, Spreemann D and Manoli Y. A cmos integrated voltage and power efficient ac/dc converter for energy harvesting applications. *J. Micromech. Microeng*, 18, 2008.

[30] W. H. Ki Y. H. Lam and C. Y. Tsui. Integrated low-loss cmos active rectifier for wirelessly powered devices. *IEEE Transactions on Circuits and Systems Part 2 Express Briefs*, 53:1378–1381, 2006.

[31] Y. Rao S. Cheng, Y. Jin and D. P. Arnold. A bridge voltage doubler ac/dc converter for low-voltage energy harvesting applications. *Tech. Dig. 9th Int. Workshop on Micro and Nanotechnology for Power Generation and Energy Conversion Apps*, pages 25–28, 2009.

[32] David P. Arnold Yuan Rao. An input-powered active ac/dc converter with zero standby power for energy harvesting applications. *2010 IEEE Energy Conversion Congress and Exposition*, pages 4441–4446, 2010.

[33] Yuan Rao and David P. Arnold Shuo Cheng, Ying Jin. An active voltage doubling ac/dc converter for low-voltage energy harvesting applications. *IEEE TRANSACTIONS ON POWER ELECTRONICS*, 26(8), 2011.

[34] A. Tabesh and L. G. Frechette. A low-power stand-alone adaptive circuit for harvesting energy from a piezoelectric micropower generator. *IEEE Trans. Ind. Electron*, 57(3):840–849, 2010.

[35] Suman Dwari Rohan Dayal and Leila Parsa. Design and implementation of a direct acdc boost converter for low-voltage energy harvesting. *IEEE TRANSACTIONS ON INDUSTRIAL ELECTRONICS*, 58(6), 2011.

[36] Acomi Ovidiu Acomi Nicoleta. Cathodic protection by sacrificial anodes or impressed current. *comparative analysis*, 19.

[37] Copper/copper sulfate reference electrode. `"http://corrosion-doctors.org/Corrosion-Thermodynamics/Reference-Half-Cells-Copper.htm"`.

[38] W. Nernst. The electromotoric effectiveness of ions. *Habilitation Thesis*, 1889.

[39] * Robert C. T. Slade Feng Zhao and John R. Varcoe. Techniques for the study and development of microbial fuel cells: an electrochemical perspective. *Chemical Society reviews*, 38(7), 2009.

[40] Juan M Feliu Eliezer Gileadi Jacek Lipkowski-Wolfgang Schmickler Sergio Trsatti Rolando Guidelli*, Richard G.Compton. Defining the transfer coeffcient in electrochemistry: An assessment(iupac technical report). *Applied Chemistry*, 86(2):245–258, 2014.

[41] S. Srinivasan J. Kim, S.M Lee. Modeling of proton exchange membrane fuel cell performance with an empirical equation. *J. Electrochem. Soc*, 142:26702674, 1995.

[42] E.P. Ambrosio M. Lucariello P. Spinelli, C. Francia. Semi-empirical evaluation of pemfc electro-catalytic activity. *J. Power Sources*, 178:517524, 2008.

[43] Moses O. Tade Valery A. Danilova. An alternative way of estimating anodic and cathodic transfer coefficients from pemfc polarization curves. *Chemical Engineering Journal*, 156:496–499, 2010.

[44] Exchange current density Wikipedia.

[45] C. W. Du Y. F. Cheng X. H. Nie, X. G. Li. Temperature dependence of the electrochemical corrosion characteristics of carbon steel in a salty soil. *J Appl Electrochem*, 39:277–282, 2009.

[46] Department of Army. Electrical design, cathodic protection. *HeadQuaters*, 1985.

[47] U.S Air Force.

[48] Line of Sight Temperature, Pitting and Graphite Anodes. `"http://www.robotroom.com/Rust-Removal-5.html"`.

[49] Ningxu Han Wei Liu Ji-Hua Zhu *, Miaochang Zhu and Feng Xing *. Electrical and mechanical performance of carbon fiber-reinforced polymer used as the impressed current anode material. *Materials*, 7:5438–5453, 2014.

[50] Pritpal S. Mangat Finbar J. OFlaherty Graeme Jones Paul Lambert, Chinh Van Nguyen. Dual function carbon fibre fabric strengthening and impressed current cathodic protection (iccp) anode for reinforced concrete structures. *Materials and Structures*, 48:21572167, 2015.

[51] DHgate.com Store. `"http://www.dhgate.com/store/product/dia-25-300mm-graphite-rods-graphite-anode/214664996.html"`.

[52] Farwest ProMag Standard Potential Magnesium Anodes Farwest corrosion control company. `"http://www.farwestcorrosion.com/promag-standard-potential-magnesium-anodes-for-soil-use.html"`.

[53] Rakman industries limied. Acsr conductor. `"http://rakman.tradeindia.com/acsr-conduction-192713.html"`.

[54] Walter Frei. Solutions to linear systems of equations: Direct and iterative solvers. `"https://www.comsol.com/blogs/solutions-linear-systems-equations-direct-iterative-solvers/"`.

[55] Wikipedia. American wire gauge. `"https://en.wikipedia.org/wiki/American_wire_gauge"`.

[56] The Mu shield company. Mu-metal specification.

[57] Texas Instruments. Tmp007. `"http://www.ti.com/product/TMP007/datasheet"`.

[58] Texas Instruments. Tmp006. `"http://www.ti.com/product/TMP006/datasheet"`.

[59] Texas Instruments. Tmp102. `"http://www.ti.com/lit/ds/symlink/tmp102.pdf"`.

[60] Air Force Manual AFM 88-9. Corrosion control. *U.S. Air Force*, 4:203, 1962.

[61] W.T. Bryan. Designing impressed current cathodic protection systems with durco anodes. *The Duriron Company*, 1970.

[62] Harco Corporation. Catalog of cathodic protection materials. 1971.

Appendix A

Mu-Metal Properties for Toroidal Core

Table A.1: AC magnetic properties, 60Hz [56]

Thickness		$\mu 40G$	$\mu 200G$	$\mu 2000G$
inch	mm			
0.025	0.635	35000	40000	55000
0.014	0.356	55000	65000	95000
0.006	0.152	65000	85000	135000
0.02	0.051	70000	90000	220000

Table A.2: Mu-metel material [56]

Carbon 0.02%	Nickel 80.00%
Manganese 0.50%	Molybdenum 4.20%
Silicon 0.35%	Iron Balanced

Appendix B

Datasheets of Several Temperature Sensors

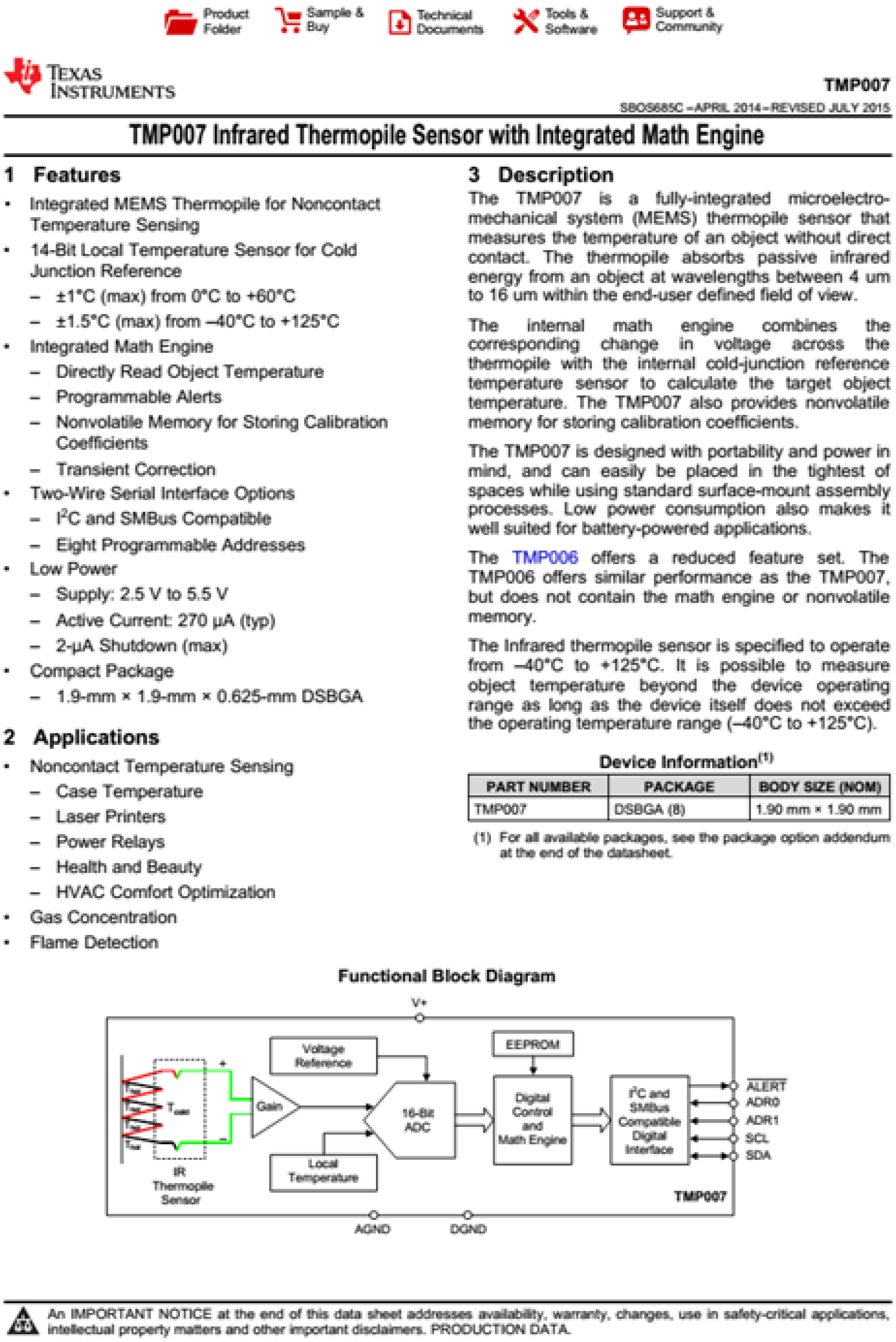

TEXAS INSTRUMENTS

TMP007

SBOS685C – APRIL 2014 – REVISED JULY 2015

TMP007 Infrared Thermopile Sensor with Integrated Math Engine

1 Features

- Integrated MEMS Thermopile for Noncontact Temperature Sensing
- 14-Bit Local Temperature Sensor for Cold Junction Reference
  - ±1°C (max) from 0°C to +60°C
  - ±1.5°C (max) from –40°C to +125°C
- Integrated Math Engine
  - Directly Read Object Temperature
  - Programmable Alerts
  - Nonvolatile Memory for Storing Calibration Coefficients
  - Transient Correction
- Two-Wire Serial Interface Options
  - I²C and SMBus Compatible
  - Eight Programmable Addresses
- Low Power
  - Supply: 2.5 V to 5.5 V
  - Active Current: 270 µA (typ)
  - 2-µA Shutdown (max)
- Compact Package
  - 1.9-mm × 1.9-mm × 0.625-mm DSBGA

2 Applications

- Noncontact Temperature Sensing
  - Case Temperature
  - Laser Printers
  - Power Relays
  - Health and Beauty
  - HVAC Comfort Optimization
- Gas Concentration
- Flame Detection

3 Description

The TMP007 is a fully-integrated microelectromechanical system (MEMS) thermopile sensor that measures the temperature of an object without direct contact. The thermopile absorbs passive infrared energy from an object at wavelengths between 4 um to 16 um within the end-user defined field of view.

The internal math engine combines the corresponding change in voltage across the thermopile with the internal cold-junction reference temperature sensor to calculate the target object temperature. The TMP007 also provides nonvolatile memory for storing calibration coefficients.

The TMP007 is designed with portability and power in mind, and can easily be placed in the tightest of spaces while using standard surface-mount assembly processes. Low power consumption also makes it well suited for battery-powered applications.

The TMP006 offers a reduced feature set. The TMP006 offers similar performance as the TMP007, but does not contain the math engine or nonvolatile memory.

The Infrared thermopile sensor is specified to operate from –40°C to +125°C. It is possible to measure object temperature beyond the device operating range as long as the device itself does not exceed the operating temperature range (–40°C to +125°C).

Device Information[1]

PART NUMBER	PACKAGE	BODY SIZE (NOM)
TMP007	DSBGA (8)	1.90 mm × 1.90 mm

(1) For all available packages, see the package option addendum at the end of the datasheet.

Functional Block Diagram

An IMPORTANT NOTICE at the end of this data sheet addresses availability, warranty, changes, use in safety-critical applications, intellectual property matters and other important disclaimers. PRODUCTION DATA.

Figure B.1: TMP007 Infrared Thermopile Sensor with Integrated Math Engine (Reprinted from [57])

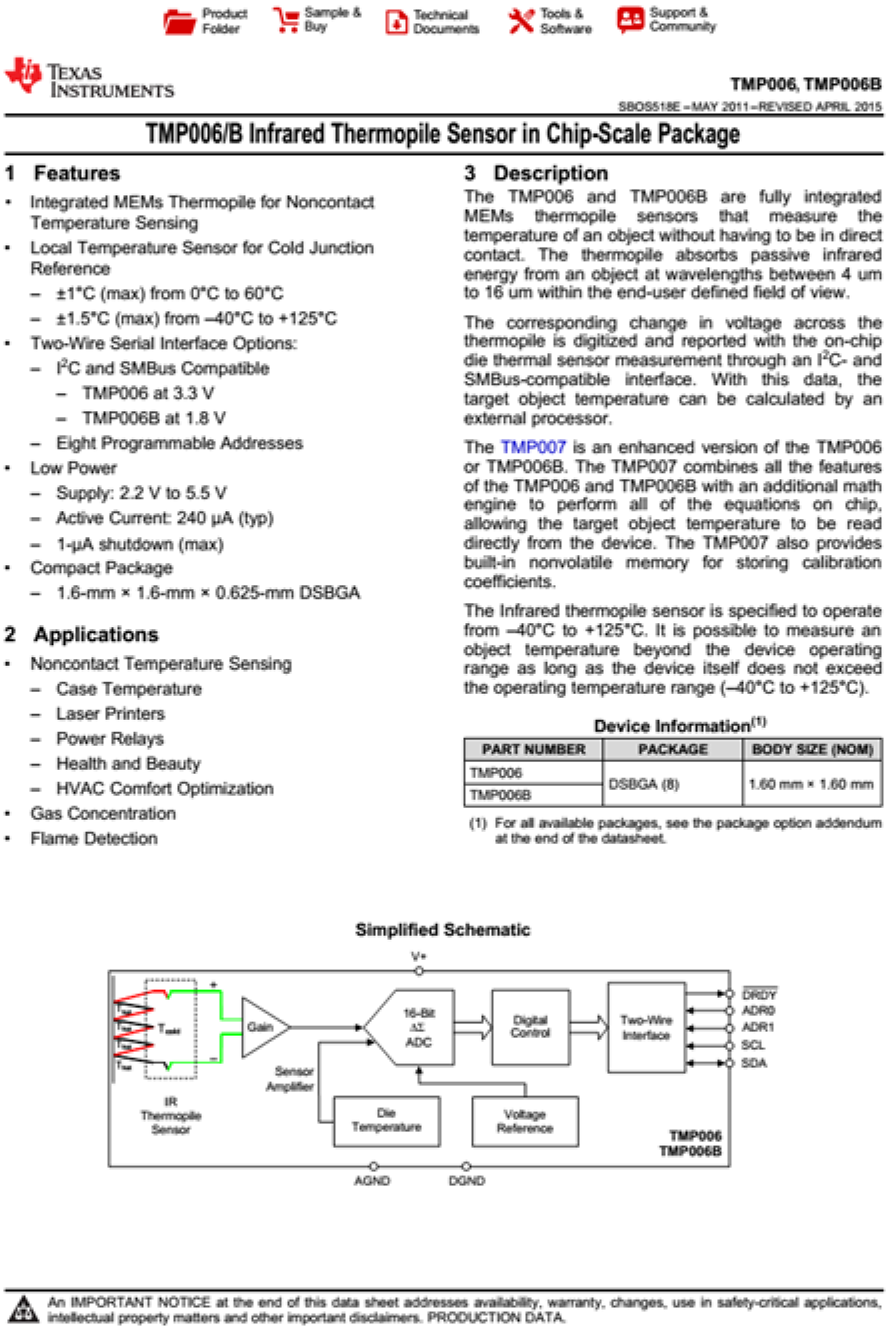

Product Folder | Sample & Buy | Technical Documents | Tools & Software | Support & Community

TEXAS INSTRUMENTS

TMP006, TMP006B

SBOS518E – MAY 2011 – REVISED APRIL 2015

TMP006/B Infrared Thermopile Sensor in Chip-Scale Package

1 Features

- Integrated MEMs Thermopile for Noncontact Temperature Sensing
- Local Temperature Sensor for Cold Junction Reference
  - ±1°C (max) from 0°C to 60°C
  - ±1.5°C (max) from –40°C to +125°C
- Two-Wire Serial Interface Options:
  - I^2C and SMBus Compatible
    - TMP006 at 3.3 V
    - TMP006B at 1.8 V
  - Eight Programmable Addresses
- Low Power
  - Supply: 2.2 V to 5.5 V
  - Active Current: 240 µA (typ)
  - 1-µA shutdown (max)
- Compact Package
  - 1.6-mm × 1.6-mm × 0.625-mm DSBGA

2 Applications

- Noncontact Temperature Sensing
  - Case Temperature
  - Laser Printers
  - Power Relays
  - Health and Beauty
  - HVAC Comfort Optimization
- Gas Concentration
- Flame Detection

3 Description

The TMP006 and TMP006B are fully integrated MEMs thermopile sensors that measure the temperature of an object without having to be in direct contact. The thermopile absorbs passive infrared energy from an object at wavelengths between 4 um to 16 um within the end-user defined field of view.

The corresponding change in voltage across the thermopile is digitized and reported with the on-chip die thermal sensor measurement through an I^2C- and SMBus-compatible interface. With this data, the target object temperature can be calculated by an external processor.

The TMP007 is an enhanced version of the TMP006 or TMP006B. The TMP007 combines all the features of the TMP006 and TMP006B with an additional math engine to perform all of the equations on chip, allowing the target object temperature to be read directly from the device. The TMP007 also provides built-in nonvolatile memory for storing calibration coefficients.

The Infrared thermopile sensor is specified to operate from –40°C to +125°C. It is possible to measure an object temperature beyond the device operating range as long as the device itself does not exceed the operating temperature range (–40°C to +125°C).

Device Information(1)

PART NUMBER	PACKAGE	BODY SIZE (NOM)
TMP006	DSBGA (8)	1.60 mm × 1.60 mm
TMP006B		

(1) For all available packages, see the package option addendum at the end of the datasheet.

Simplified Schematic

An IMPORTANT NOTICE at the end of this data sheet addresses availability, warranty, changes, use in safety-critical applications, intellectual property matters and other important disclaimers. PRODUCTION DATA.

Figure B.2: TMP006/B Infrared Thermopile Sensor in Chip-Scale Package (Reprinted from [58])

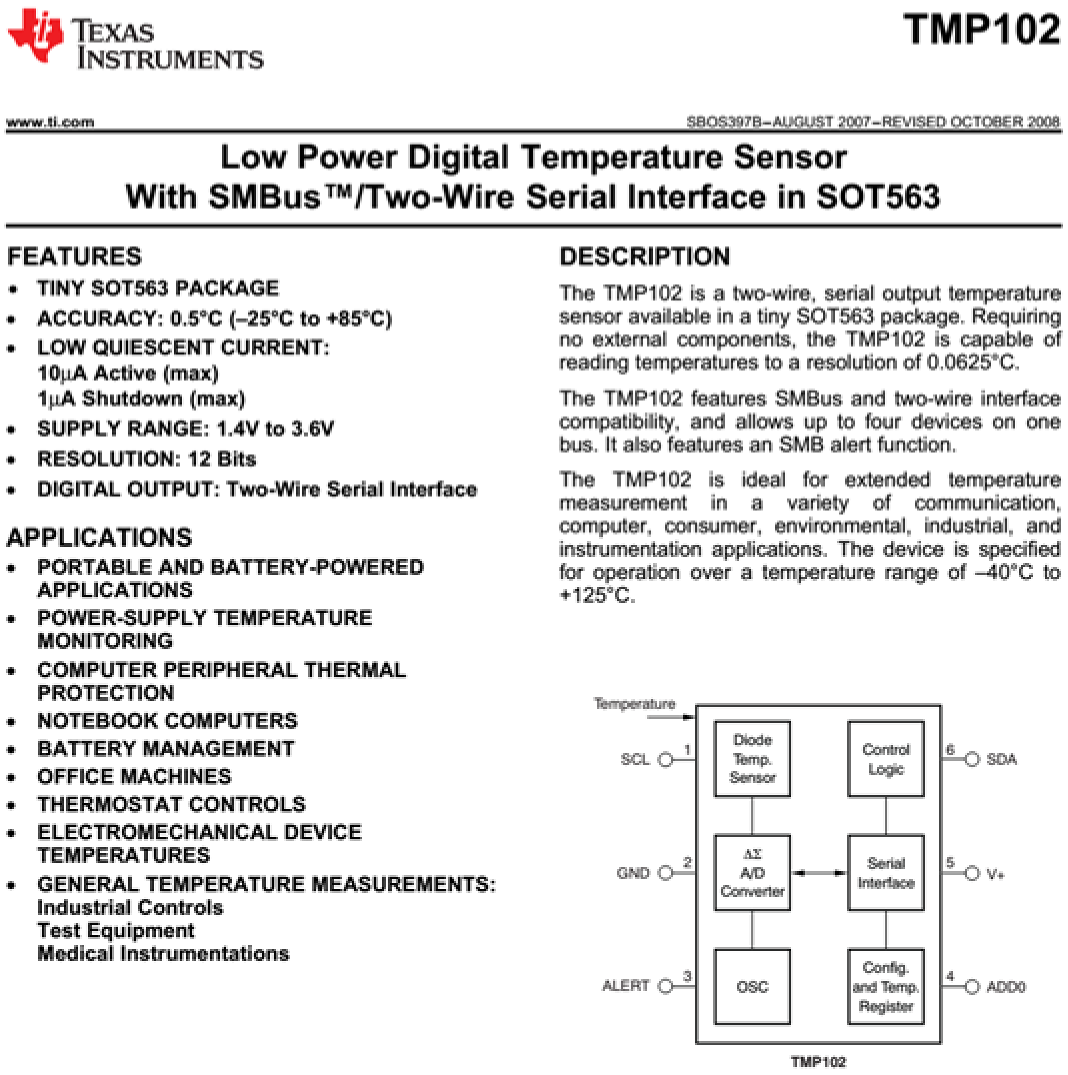

TEXAS INSTRUMENTS

TMP102

www.ti.com

SBOS397B–AUGUST 2007–REVISED OCTOBER 2008

Low Power Digital Temperature Sensor
With SMBus™/Two-Wire Serial Interface in SOT563

FEATURES

- TINY SOT563 PACKAGE
- ACCURACY: 0.5°C (–25°C to +85°C)
- LOW QUIESCENT CURRENT:
  10µA Active (max)
  1µA Shutdown (max)
- SUPPLY RANGE: 1.4V to 3.6V
- RESOLUTION: 12 Bits
- DIGITAL OUTPUT: Two-Wire Serial Interface

APPLICATIONS

- PORTABLE AND BATTERY-POWERED APPLICATIONS
- POWER-SUPPLY TEMPERATURE MONITORING
- COMPUTER PERIPHERAL THERMAL PROTECTION
- NOTEBOOK COMPUTERS
- BATTERY MANAGEMENT
- OFFICE MACHINES
- THERMOSTAT CONTROLS
- ELECTROMECHANICAL DEVICE TEMPERATURES
- GENERAL TEMPERATURE MEASUREMENTS:
  Industrial Controls
  Test Equipment
  Medical Instrumentations

DESCRIPTION

The TMP102 is a two-wire, serial output temperature sensor available in a tiny SOT563 package. Requiring no external components, the TMP102 is capable of reading temperatures to a resolution of 0.0625°C.

The TMP102 features SMBus and two-wire interface compatibility, and allows up to four devices on one bus. It also features an SMB alert function.

The TMP102 is ideal for extended temperature measurement in a variety of communication, computer, consumer, environmental, industrial, and instrumentation applications. The device is specified for operation over a temperature range of –40°C to +125°C.

Figure B.3: Low power digital temperature sensor with SMBus/Two-Wire serial interface in SOT563 (Reprinted from [59])

Appendix C

Parameters for Analysis Cathodic Protection

Table C.1: Tested current density for cathodic corrosion on uncoated steel [60]

Environment	Current density (mA/sq ft)
Neutral soil%	0.5-1.5
Well aerated neutral soil	2-3
Wet soil	1-6
Highly acidic soil	3-15
Soil supporting active sulfate-reducing bacteria	6-42
Heated soil	3-25
Stationary fresh water	1-6
Moving fresh water containing dissolved oxygen	5-15
Seawater	3-10

Table C.2: Shape function K for ICCP while L is effective anode length, d is anode backfill length[61]

L/d	K	L/d	K
5	0.0140	14	0.0194
6	0.0150	16	0.0201
7	0.0158	20	0.0213
8	0.0165	25	0.0224
9	0.0171	30	0.0234
10	0.0177	35	0.0242
12	0.0186	40	0.0249

Table C.4: Weight and dimensions for high silicon chromium bear cast iron anodes[62]

Anode weight (lb)	Anode dimensions (in)	Anode surface size (in)	Package area (sq ft)
12	1*60	1.4	10*84
44	2*60	2.6	10*84
60	2*60	2.8	10*84
110	3*60	4.0	10*84

Table C.3: Anode paralleling number for various number of anodes set in parallel[61]

N	P	N	P
2	0.00261	14	0.00168
3	0.00289	16	0.00155
4	0.00283	18	0.00145
5	0.00268	20	0.00135
6	0.00252	22	0.00128
7	0.00237	24	0.00121
8	0.00224	26	0.00114
9	0.00212	28	0.00109
10	0.00201	30	0.00104
12	0.00182		

Appendix D

Steps for Building 3D Energy Harvester Model in COMSOL

A 3D geometry model can be built in SolidWorks by the following steps:

1. Draw a circle for the cross section of ASCR cable on top plane, and extrude the circle by typing the length of the cable. The length should not be too long which will create too many elements, or too short that can compare to the length of the magnetic core. A length that is three to four times the length of the magnetic core is fine for simulation.

2. Set a new script on right plane and draw a rectangular cross section for magnetic core, the outer boundary will be 50.8mm away from the z-axis, then use rotate to let rectangle rotate around the z-axis. The finished core is shown in Figure D.1 below.

3. Cut the core gap for the core on the top plane script if needed. Choose the core geometry and create an offset surface for it. The distance between the offset surface and the surface of the core is set for 1mm for the reason the coil should not be too far away form the core and the distance will not make the mesh for simulation too burdensome.

4. Locate the top plane and create a new script, draw two straight lines continuously on the radius direction, one start from the center of the circle to the middle of the width of the core, the other start from the middle of the core to an end point. The length of the second line should be longer than the half of the length of core.

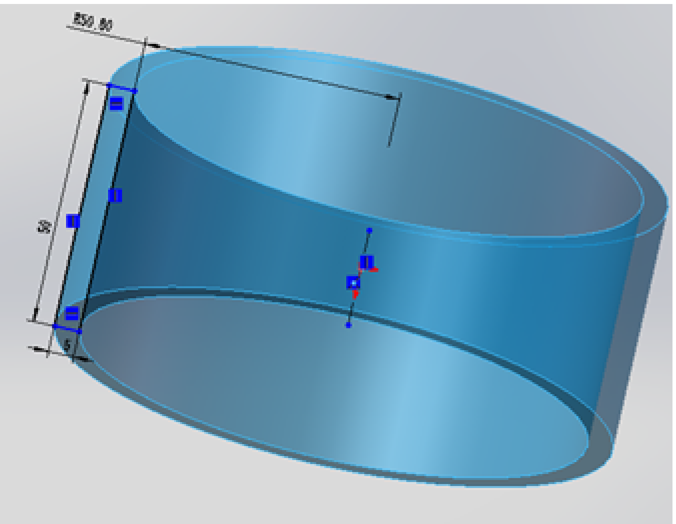

Figure D.1: A geometry for magnetic core is created after rotating a rectangle

5. Set the second line drawn in step 4 as a constructive line, draw an arc with radius from z-axis to the half width of the core and set it as path. The orientation for constructive line is twist along the path and set the turns 50, the result is shown in Figure D.2 below.

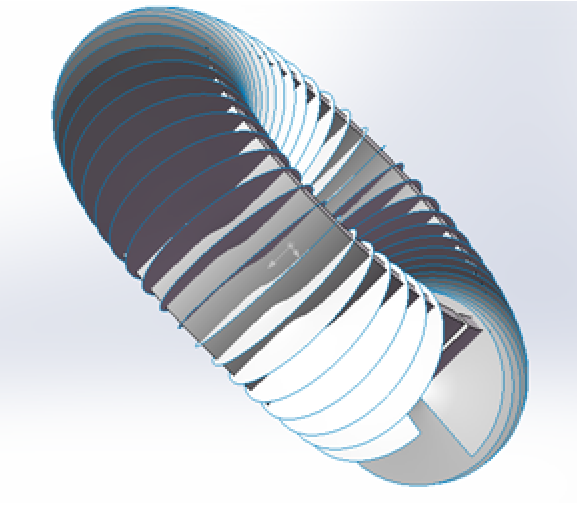

Figure D.2: Constructive line twist around the path

6. Using fillet to trim the edge of core when offset surface is shown in order to make the coil created in the next step not too sharp to mesh before simulation. Choose both the offset surface and the twisted surface, then use intersection curve to obtain the intersection curves wounding around the offset surface.

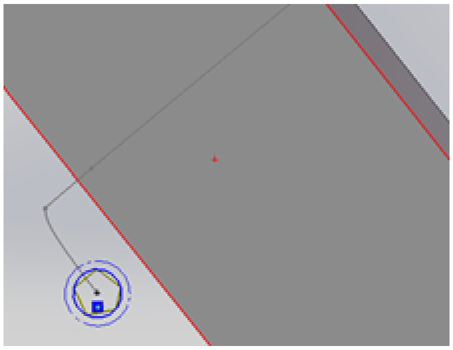

Figure D.3: Initial circle as cross section of coil for sweep

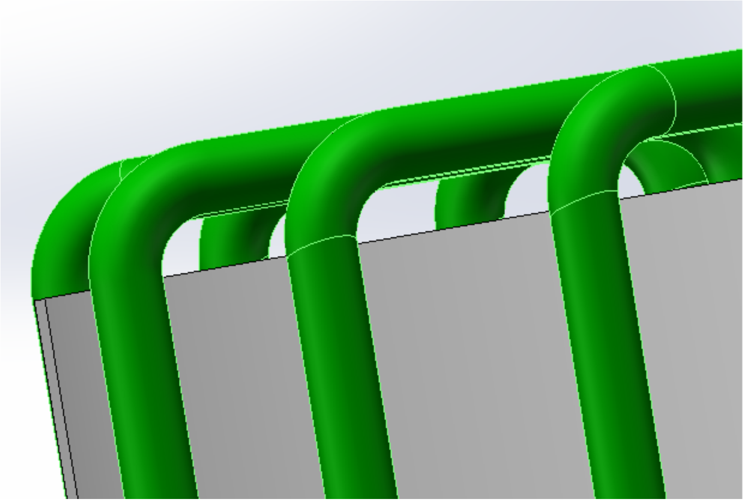

Figure D.4: Coil is generated after sweep along path

7. Then draw a circle centered on the start point of the intersection curve as shown in Figure D.3 and use sweep to let the circle goes through the intersection curve in order to get the coil geometry shown in Figure D.4.

8. Hide the offset surface and color the coil and the core, the final structure result in Figure D.5 can be imported to COMSOL directly.

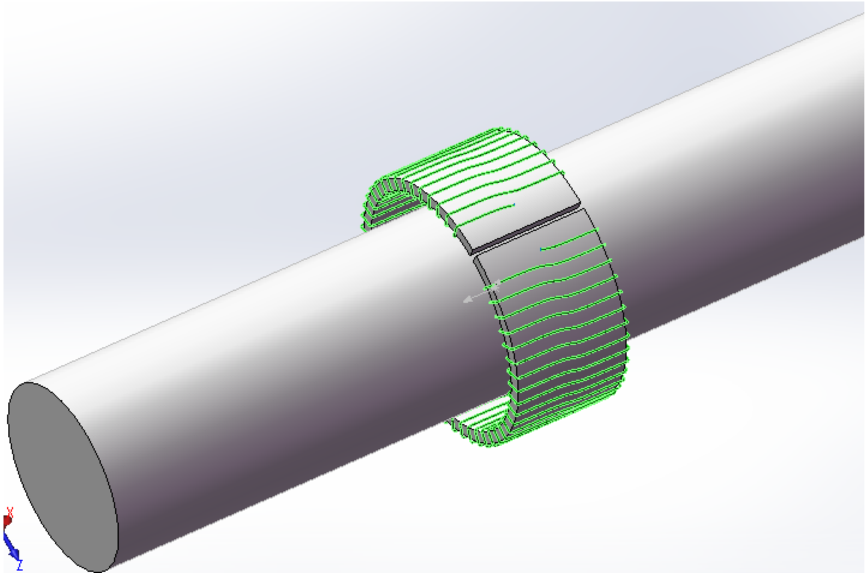

Figure D.5: Final result of geometry of energy harvester